

# A selectively reduced degree basis for efficient mixed nonlinear isogeometric beam formulations with extensible directors

Myung-Jin Choi<sup>a,\*</sup>, Roger A. Sauer<sup>b,c,d</sup>, Sven Klinkel<sup>a</sup>

<sup>a</sup>*Chair of Structural Analysis and Dynamics, RWTH Aachen University, Mies-van-der-Rohe Str. 1, 52074 Aachen, Germany*

<sup>b</sup>*Aachen Institute for Advanced Study in Computational Engineering Science (AICES), RWTH Aachen University, Templergraben 55, 52062 Aachen, Germany*

<sup>c</sup>*Faculty of Civil and Environmental Engineering, Gdańsk University of Technology, ul. Narutowicza 11/12, 80-233 Gdańsk, Poland*

<sup>d</sup>*Department of Mechanical Engineering, Indian Institute of Technology Guwahati, Assam 781039, India*

---

## Abstract

The effect of higher order continuity in the solution field by using NURBS basis function in isogeometric analysis (IGA) is investigated for an efficient mixed finite element formulation for elastostatic beams. It is based on the Hu-Washizu variational principle considering geometrical and material nonlinearities. Here we present a reduced degree of basis functions for the additional fields of the stress resultants and strains of the beam, which are allowed to be discontinuous across elements. This approach turns out to significantly improve the computational efficiency and the accuracy of the results. We consider a beam formulation with extensible directors, where cross-sectional strains are enriched to avoid Poisson locking by an enhanced assumed strain method. In numerical examples, we show the superior per degree-of-freedom accuracy of IGA over conventional finite element analysis, due to the higher order continuity in the displacement field. We further verify the efficient rotational coupling between beams, as well as the path-independence of the results.

*Keywords:* Beam structures, Mixed formulation, Isogeometric analysis, Nonlinearity, Rotational continuity, Path-independence

---

## 1. Introduction

Beam models have been widely utilized for an efficient and accurate mechanical simulation of slender rods, rod-like bodies, and their assemblies, across many application areas, see e.g., simulations of Brownian dynamics of microstructures (Cyron and Wall, 2012), atomistic structures (Schmidt et al., 2015), and entangled materials (Durville, 2005). Accordingly, many beam models have been developed, whose applicability is, however, often limited by a certain range of geometrical characteristics of the beam, e.g. the slenderness ratio, and the cross-sectional shape. For an extensive classification of linear and nonlinear beam theories, we refer readers to the recent review in Meier et al. (2019). In this paper, we aim at expanding the applicability of our nonlinear beam formulation from previous work (Choi et al., 2021)

---

\*Corresponding author

*Email addresses:* [choi@lbb.rwth-aachen.de](mailto:choi@lbb.rwth-aachen.de) (Myung-Jin Choi), [sauer@aices.rwth-aachen.de](mailto:sauer@aices.rwth-aachen.de) (Roger A. Sauer), [klinkel@lbb.rwth-aachen.de](mailto:klinkel@lbb.rwth-aachen.de) (Sven Klinkel)

to the thin beam limit, with much improved robustness and efficiency. In this paper, we particularly investigate the effect of higher order continuity in the displacement, and director fields, in the framework of isogeometric analysis (IGA), using non-uniform rational B-splines (NURBS) basis functions.

Isogeometric analysis was presented by [Hughes et al. \(2005\)](#) to incorporate the exact geometrical description, inherent in computer-aided design (CAD) model, into analysis, by employing the same spline basis functions utilized in CAD system. This approach enables not only the exact description of the initial geometry, but also the higher order continuity in the solution field. In this study, we focus on the superiority of the  $k$ -version of mesh refinement (smooth degree elevation) in IGA in terms of per DOF accuracy in elastostatic nonlinear beam problems. We compare the results with conventional FEA with Lagrange shape functions. For further extension to dynamic problems like structural vibration and wave propagation, one may refer to [Hughes et al. \(2008\)](#). The smoothness property in IGA enables us to use much less DOFs per element, compared with conventional FEA. To simply illustrate this attractive property, we consider a mesh in a one-dimensional domain. For  $C^0$ -continuous finite elements, the number of nodes (or basis functions) is expressed by

$$n_{\text{nd}} = p \cdot n_{\text{el}} + 1, \quad (1)$$

where  $p$  and  $n_{\text{el}}$  denote the degree of basis functions, and the number of elements, respectively. In contrast, for  $C^{p-1}$ -continuous IGA, the number of control points (or basis functions) is

$$n_{\text{cp}} = n_{\text{el}} + p. \quad (2)$$

That is, as we increase the number of elements ( $n_{\text{el}}$ ), the increase in the number of nodes in FEA is much larger than that in IGA, and this gap increases as we choose higher  $p$ . This property simply extends to multi-dimensional cases, see, e.g., [Cottrell et al. \(2006\)](#). However, it turns out that IGA also suffers from numerical locking ([Echter and Bischoff, 2010](#)) in constrained problems like bending-dominated slender beams. It was also shown that the higher order continuity in the displacement and rotation fields may accenuate the locking ([Adam et al., 2014](#)).

Locking can be attributed to a *field-inconsistency* in the approximated strains in the conventional displacement-based finite element formulation ([Prathap, 2013](#)). In order to alleviate locking, many approaches have been developed, which include reduced integration methods, and mixed variational formulations. In the framework of IGA, they can be divided into *local* (element-wise) and *global* (patch-wise) approaches. An *element-wise* selective and reduced integration (SRI) method falls into the first category. A SRI rule for quadratic NURBS basis functions was presented in [Bouclier et al. \(2012\)](#), and it was generalized by [Adam et al. \(2014\)](#) in terms of the degree of basis functions and the inter-element continuity. A key observation of the latter work is that additional constraints in the stiffness matrix may arise due to higher inter-element continuity in the membrane and transverse shear strain fields, which can also lead to a significant spurious increase of the bending stiffness. Thus, for IGA, a local approach always needs to be combined with an additional treatment, e.g., further reduction of the number of quadrature points in the SRI, see [Adam et al. \(2014\)](#). A local approach can be also found in the context of  $\bar{B}$  projection methods for IGA. For example, [Hu et al. \(2016\)](#) presented a selective reduction of the

degree of basis in the local (element-wise) projection space, which was extended to shell problems in [Hu et al. \(2020\)](#). On the other hand, a *patch-wise* quadrature rule, which falls into the global approach, was initiated by an observation that the conventional element-wise quadrature rule for FEA may not be optimal for IGA ([Hughes et al., 2010](#)). Patch-wise reduced integration approaches to alleviate locking were also developed, e.g., SRI in [Adam et al. \(2015\)](#), and a Greville quadrature rule in [Zou et al. \(2022\)](#). A global approach in mixed formulations suffers from a significant increase of the computational cost due to the inversion of the global Gram matrix, and the resulting *dense* global stiffness matrix, see, e.g., the  $\bar{B}$  projection method in [Bouclier et al. \(2012\)](#). To overcome this, a local least square (LLSQ) method ([Govindjee et al., 2012](#)) was employed in [Bouclier et al. \(2013\)](#). We first recall the solution process in LLSQ<sup>1</sup>. It converts the given least square problem to find the solution  $u_F$  into an approximated problem, which can be solved much more efficiently.

$$Gu_F = p \Leftrightarrow G_E A^T u_F = p_E + q, \quad q \in \ker(A) \Rightarrow G_E A^T u_S = p_E \Leftrightarrow u_S = \underbrace{(AA^T)^{-1}}_{\text{diag.}} A G_E^{-1} p_E, \quad (3)$$

where  $G_E$  is a block diagonal matrix, whose blocks are element-wise Gram matrices, and  $A$  denotes the assembly operator (Boolean matrix). By neglecting  $q$ , which is a kernel of the matrix  $A$ , a set of independent *element-wise* equations is obtained, whose solution  $u_S$  is an approximation of the original solution  $u_F$ , i.e.,  $u_S \neq u_F$ . Note that in the calculation of  $u_S$ , the matrices that need to be inverted are the diagonal matrix,  $AA^T$ , and the element Gram matrices, which is much more efficient than inverting the global Gram matrix  $G$ . Although neglecting  $q$  gives a significant improvement in the efficiency, the error  $\|u_S - u_F\|$  may increase, as degree of basis  $p$  and the inter-element continuity increase. A similar concept was employed in the mixed formulation for alleviating membrane locking in plane Kirchhoff rods by [Greco et al. \(2017\)](#). This approach was extended to shell problems in [Kikis and Klinkel \(2022\)](#), based on the Hellinger-Reissner variational principle, where the test functions are allowed to have discontinuities, so that the finite element equations for the test functions of the additional solution fields can be treated independently from each other. This enables an efficient element-wise static condensation. However, this selection of different function spaces for the test functions and solutions leads to unsymmetric stiffness matrix. A mixed formulation was also developed in the context of isogeometric collocation method for nonlinear beams, e.g., [Marino \(2017\)](#) and [Weeger et al. \(2017\)](#), where the control variables of the additional fields are not condensed out, which may significantly increase the number of DOFs, but the stiffness matrix is still sparse. A more intuitive way to achieve field-consistency, in geometrically linear problems, is to utilize one degree lower bases for the rotation field, e.g., see [Da Veiga et al. \(2012\)](#) for plate problems and [Kikis et al. \(2019\)](#) for plate and shell problems.

A beam can be regarded as a spatial curve with attached deformable director vectors (or *directors*). This curve is then also called *directed* or *Cosserat* curve. In this paper, the mixed formulation is based on the first order beam kinematics in [Choi et al. \(2021\)](#), where it was shown that the displacement-based beam formulation suffers from transverse shear, membrane, and curvature-thickness locking. For an illustration of the curvature-thickness locking, one may refer to [Betsch and Stein \(1995\)](#). It was also

<sup>1</sup>Here we recall Eqs. (8) and (9) in [Govindjee et al. \(2012\)](#), and use  $(\bullet)^T$  for the matrix transpose.

observed that the tangent stiffness matrix becomes ill-conditioned in the thin beam limit, which leads to instability in the Newton-Raphson solution process. In our present study, a Hu-Washizu variational principle is employed, where we introduce additional solution fields for the stress resultants and strains of the beam. This provides the following advantages:

- Alleviation of transverse shear, membrane, and curvature-thickness locking,
- Improved convergence of the Newton-Raphson iteration for larger load increments (Klinkel et al., 2006), and in the thin beam limit,
- In contrast to the Hellinger-Reissner principle, the stress resultants and strain of the beam are independent from each other, so that we can use nonlinear constitutive laws (Santos et al., 2010).

Our mixed formulation is basically a *local approach*, and we alleviate the additional artificial constraints due to the higher order continuity, by reducing the degree of basis functions in the additional solution fields, i.e., the beam's stress resultants and strains. This approach has the following novelties over previous local and global approaches:

- It enables an element-wise static condensation.
- It reduces the number of internal variables, and the size of relevant stiffness (sub-)matrices, which also makes the matrix operations in the condensation process computationally more efficient.
- It uses the same function space for the test and solution functions of the additional fields, so that the resulting stiffness matrix is always symmetric.<sup>2</sup>

The remainder of this paper is organized as follows. In Section 2, we briefly review the beam kinematics with extensible directors, and recall the expressions of the strains, and the stress resultants of the beam. In Section 3, we present a mixed finite element formulation, based on the Hu-Washizu variational principle. In Section 4, we present the isogeometric finite element discretization. In Section 5, we present a formulation for imposing the rotational continuity between beams. In Section 6, several numerical examples are presented. Section 7 concludes the paper.

## 2. Beam kinematics

Two transverse directions of the beam are defined by the principal directions of the second moment of inertia tensor in the initial (undeformed) cross-section. The origin of the transverse coordinates  $\zeta^\alpha$  ( $\alpha \in \{1, 2\}$ ) is defined by the geometrical center of the initial cross-section, which coincides with the mass center under the assumption of constant mass density in the initial configuration. The line connecting these center points of the cross-sections is called an axis, whose position is denoted by  $\varphi(s, t)$ .

---

<sup>2</sup>Here we assume conservative loads, and no rotational coupling conditions. The relevant discussions are given in Sections 3 and 5, respectively.

Here,  $s$  denotes the arc-length coordinate along the initial center axis, and  $t$  denotes time. In this paper, the argument  $t$  is often omitted for brevity. The initial beam configuration is expressed by

$$\mathbf{x}_0(\zeta^1, \zeta^2, s) = \boldsymbol{\varphi}_0(s) + \zeta^\gamma \mathbf{D}_\gamma(s), \quad (4)$$

where  $\boldsymbol{\varphi}_0(s)$  denotes the position of the beam's initial center axis, and the initial cross-sectional plane is spanned by two *initial directors*  $\mathbf{D}_\gamma(s) \in \mathbb{R}^3$  ( $\gamma \in \{1, 2\}$ ). Here and hereafter, unless stated otherwise, repeated Greek indices like  $\alpha, \beta$ , and  $\gamma$  imply summation over 1 to 2, and repeated Latin indices like  $i$  and  $j$  imply summation over 1 to 3. We define a covariant basis  $\mathbf{G}_i := \partial \mathbf{x}_0 / \partial \zeta^i$  ( $i \in \{1, 2, 3\}$ ) with  $\zeta^3 \equiv s$ , and a contravariant basis  $\{\mathbf{G}^1, \mathbf{G}^2, \mathbf{G}^3\}$  is defined by the orthogonality condition  $\mathbf{G}_i \cdot \mathbf{G}^j = \delta_i^j$ , where  $\delta_i^j$  denotes the Kronecker-delta. According to the first order beam kinematics (Rhim and Lee, 1998; Choi et al., 2021), the position vector is a linear function of the coordinates  $\zeta^\gamma$  along the transverse directions, i.e.

$$\mathbf{x}(\zeta^1, \zeta^2, s, t) = \boldsymbol{\varphi}(s, t) + \zeta^\gamma \mathbf{d}_\gamma(s, t), \quad (5)$$

where  $\boldsymbol{\varphi}(s, t)$  denotes the current position of the center axis, and the current cross-sectional plane is spanned by two *current directors*  $\mathbf{d}_\gamma(s, t) \in \mathbb{R}^3$  ( $\gamma \in \{1, 2\}$ ). Fig. 1 schematically illustrates this beam kinematics. Fig. 2 shows a reference domain in the case of a rectangular cross-section, where  $\{\mathbf{E}_1, \mathbf{E}_2, \mathbf{E}_3\}$  denotes the standard Cartesian basis in  $\mathbb{R}^3$ , with  $\mathbf{E}_3$  along the axial direction, and  $\mathbf{E}_1$  and  $\mathbf{E}_2$  along two transverse directions.

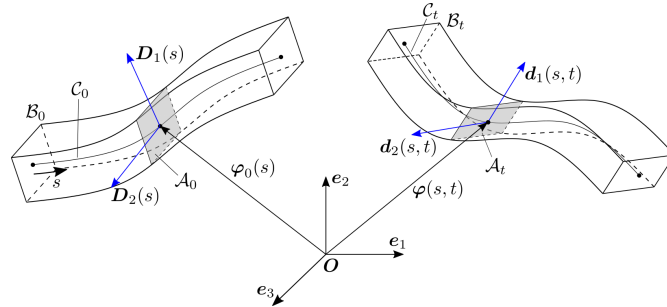


Figure 1: An illustration of the beam kinematics in the initial and current configurations, whose domains are denoted by  $\mathcal{B}_0$  and  $\mathcal{B}_t$ , respectively.  $\mathcal{C}_0$  and  $\mathcal{C}_t$  indicate the initial and current center axes, respectively.  $\mathcal{A}_0$  and  $\mathcal{A}_t$  indicate the initial and current cross-sections, respectively.  $\{\mathbf{e}_1, \mathbf{e}_2, \mathbf{e}_3\}$  denotes the standard Cartesian basis in  $\mathbb{R}^3$ . This figure is redrawn with modifications from Choi et al. (2021).

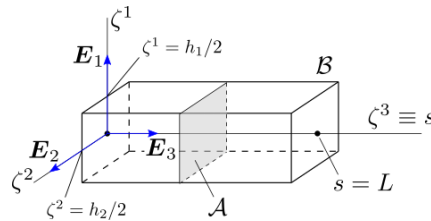


Figure 2: An example of the reference domain  $\mathcal{B}$  having a rectangular cross-section with dimension  $h_1 \times h_2$ .  $\mathcal{A}$  denotes the reference domain of the cross-section. This figure is redrawn with modifications from Choi et al. (2021).

The covariant components of the Green-Lagrange strain tensor  $\mathbf{E} = E_{ij} \mathbf{G}^i \otimes \mathbf{G}^j$  can be expressed in

terms of the beam strains, as (Choi et al., 2021)

$$\underline{\mathbf{E}} = \begin{bmatrix} 0 & 0 & 0 & 0 & 0 & 0 & 0 & 0 & 0 & 0 & 0 & 0 & 1 & 0 & 0 \\ 0 & 0 & 0 & 0 & 0 & 0 & 0 & 0 & 0 & 0 & 0 & 0 & 0 & 1 & 0 \\ 1 & \zeta^1 & \zeta^2 & \zeta^1\zeta^1 & \zeta^2\zeta^2 & \zeta^1\zeta^2 & 0 & 0 & 0 & 0 & 0 & 0 & 0 & 0 & 0 \\ 0 & 0 & 0 & 0 & 0 & 0 & 0 & 0 & 0 & 0 & 0 & 0 & 0 & 0 & 1 \\ 0 & 0 & 0 & 0 & 0 & 0 & 1 & 0 & \zeta^1 & \zeta^2 & 0 & 0 & 0 & 0 & 0 \\ 0 & 0 & 0 & 0 & 0 & 0 & 0 & 1 & 0 & 0 & \zeta^1 & \zeta^2 & 0 & 0 & 0 \end{bmatrix} \begin{Bmatrix} \varepsilon \\ \boldsymbol{\rho} \\ \boldsymbol{\kappa} \\ \boldsymbol{\delta} \\ \boldsymbol{\gamma} \\ \boldsymbol{\chi} \end{Bmatrix} =: \mathbf{A}\boldsymbol{\varepsilon}, \quad (6)$$

with  $\underline{\mathbf{E}} := [E_{11}, E_{22}, E_{33}, 2E_{12}, 2E_{13}, 2E_{23}]^T$ , where we have defined the beam strain arrays

$$\boldsymbol{\rho} := \begin{Bmatrix} \rho_1 \\ \rho_2 \end{Bmatrix}, \quad \boldsymbol{\kappa} := \begin{Bmatrix} \kappa_{11} \\ \kappa_{22} \\ 2\kappa_{12} \end{Bmatrix}, \quad \boldsymbol{\delta} := \begin{Bmatrix} \delta_1 \\ \delta_2 \end{Bmatrix}, \quad \boldsymbol{\gamma} := \begin{Bmatrix} \gamma_{11} \\ \gamma_{12} \\ \gamma_{21} \\ \gamma_{22} \end{Bmatrix}, \quad \text{and } \boldsymbol{\chi} := \begin{Bmatrix} \chi_{11} \\ \chi_{22} \\ 2\chi_{12} \end{Bmatrix},$$

with

$$\varepsilon := \frac{1}{2}(\|\boldsymbol{\varphi}_{,s}\|^2 - 1) \quad (\text{axial stretching strain}), \quad (7a)$$

$$\rho_\alpha := \boldsymbol{\varphi}_{,s} \cdot \mathbf{d}_{\alpha,s} - \boldsymbol{\varphi}_{0,s} \cdot \mathbf{D}_{\alpha,s} \quad (\text{bending strain}), \quad (7b)$$

$$\delta_\alpha := \boldsymbol{\varphi}_{,s} \cdot \mathbf{d}_\alpha - \boldsymbol{\varphi}_{0,s} \cdot \mathbf{D}_\alpha \quad (\text{transverse shear strain}), \quad (7c)$$

$$\gamma_{\alpha\beta} := \mathbf{d}_\alpha \cdot \mathbf{d}_{\beta,s} - \mathbf{D}_\alpha \cdot \mathbf{D}_{\beta,s} \quad (\text{couple shear strain}), \quad (7d)$$

$$\chi_{\alpha\beta} := \frac{1}{2}(\mathbf{d}_\alpha \cdot \mathbf{d}_\beta - \mathbf{D}_\alpha \cdot \mathbf{D}_\beta) \quad (\text{cross-section stretching and in-plane shear strains}), \quad (7e)$$

$$\kappa_{\alpha\beta} := \frac{1}{2}(\mathbf{d}_{\alpha,s} \cdot \mathbf{d}_{\beta,s} - \mathbf{D}_{\alpha,s} \cdot \mathbf{D}_{\beta,s}) \quad (\text{high-order bending strain}). \quad (7f)$$

**Remark 2.1.** *Constant in-plane cross-sectional strains in the beam kinematics.* Two extensible directors can represent constant in-plane cross-sectional strains according to Eq. (7e), and the work-conjugate stress resultants may not vanish as well. That is, the conventional zero-stress condition is not imposed here. The inability to represent linear in-plane (cross-sectional) strains may artificially increase the bending stiffness, which is so called *Poisson locking*. In Section 3.1, we discuss the further enrichment of the cross-sectional strain, based on the EAS method.

### 3. Mixed finite element formulation

#### 3.1. Variational formulation

We assume that the *strain energy density* (defined as the strain energy per unit undeformed volume) is expressed in terms of the Green-Lagrange strain tensor  $\mathbf{E} = \mathbf{E}(\mathbf{u})$  with  $\mathbf{u} := \mathbf{x} - \mathbf{x}_0$ , as

$$\Psi = \Psi(\mathbf{E}). \quad (8)$$

Then the total strain energy of the beam is obtained from

$$U := \int_{\mathcal{B}_0} \Psi \, d\mathcal{B}_0 = \int_0^L \int_{\mathcal{A}} \Psi \, j_0 \, d\mathcal{A} \, ds, \quad (9)$$

where  $j_0$  denotes the Jacobian of the mapping  $\mathbf{x}_0(\zeta^1, \zeta^2, s) : \mathcal{B} \rightarrow \mathcal{B}_0$ , such that  $d\mathcal{B}_0 = j_0 d\mathcal{B}$ . In the Hu-Washizu variational principle, the total strain energy is expressed by

$$U_{\text{HW}} := \int_0^L \int_{\mathcal{A}} \Psi_{\text{HW}} j_0 d\mathcal{A} ds, \quad (10)$$

with the strain energy density,

$$\Psi_{\text{HW}} = \Psi_{\text{HW}}(\mathbf{E}(\mathbf{u}), \mathbf{E}_p, \mathbf{S}_p) = \Psi(\mathbf{E}_p) + \mathbf{S}_p : \{\mathbf{E}(\mathbf{u}) - \mathbf{E}_p\}, \quad (11)$$

where we have three independent solution fields, the displacement vector  $\mathbf{u}$ , the *physical* Green-Lagrange strain tensor  $\mathbf{E}_p$ , and the *physical* second Piola-Kirchhoff stress tensor  $\mathbf{S}_p$ .  $\mathbf{E}(\mathbf{u})$  denotes the *geometrical* (or compatible) Green-Lagrange strain tensor. The physical Green-Lagrange strain can be decomposed into the *physical kinematic* part, and the *enhanced* part, as (Simo and Rifai, 1990)

$$\mathbf{E}_p = \underbrace{\mathbf{E}_p^c}_{\text{kinematic}} + \underbrace{\tilde{\mathbf{E}}}_{\text{enhanced}}, \quad (12)$$

where the additional strain part  $\tilde{\mathbf{E}}$  is intended to enrich higher-order cross-sectional strains. It is noted that, in contrast to the beam formulation of Wackerfuß and Gruttmann (2009), which considers no cross-sectional strains (rigid cross-section) in the kinematic assumption, the kinematic part in Eq. (12) includes a constant in-plane strain field, see Remark 2.1. From Eq. (6), the physical kinematic part can be further decomposed into

$$\underline{\mathbf{E}}_p^c(\zeta^1, \zeta^2, s) = \mathbf{A}(\zeta^1, \zeta^2) \boldsymbol{\varepsilon}_p(s), \quad (13)$$

where  $\boldsymbol{\varepsilon}_p(s)$  denotes the array of physical (kinematic) beam strains, i.e.  $\boldsymbol{\varepsilon}_p := [\varepsilon_p, \boldsymbol{\rho}_p^T, \boldsymbol{\kappa}_p^T, \boldsymbol{\delta}_p^T, \boldsymbol{\gamma}_p^T, \boldsymbol{\chi}_p^T]^T$ . Note that we use  $\underline{(\bullet)}$  to denote the Voigt notation of a second order tensor. The enhanced part is decomposed into

$$\underline{\tilde{\mathbf{E}}}(\zeta^1, \zeta^2, s) = \boldsymbol{\Gamma}(\zeta^1, \zeta^2) \boldsymbol{\alpha}(s). \quad (14)$$

In order to alleviate Poisson locking, we enrich the linear and bilinear strains in the cross-section, using the polynomial basis functions

$$\boldsymbol{\Gamma}(\zeta^1, \zeta^2) := \begin{bmatrix} \zeta^1 & \zeta^2 & \zeta^1\zeta^2 & 0 & 0 & 0 & 0 & 0 & 0 \\ 0 & 0 & 0 & \zeta^1 & \zeta^2 & \zeta^1\zeta^2 & 0 & 0 & 0 \\ 0 & 0 & 0 & 0 & 0 & 0 & 0 & 0 & 0 \\ 0 & 0 & 0 & 0 & 0 & 0 & \zeta^1 & \zeta^2 & \zeta^1\zeta^2 \\ 0 & 0 & 0 & 0 & 0 & 0 & 0 & 0 & 0 \\ 0 & 0 & 0 & 0 & 0 & 0 & 0 & 0 & 0 \end{bmatrix}, \quad (15)$$

with nine coefficient functions  $\alpha_i(s)$ ,  $i \in \{1, 2, \dots, 9\}$  (Choi et al., 2021). Here, we enrich only the linear and bilinear in-plane cross-sectional strains, i.e.  $E_{11}$ ,  $E_{12}$ , and  $E_{22}$ . For further enrichment of higher order strains including the out-of-plane ones, one may refer to Wackerfuß and Gruttmann (2009) and Wackerfuß and Gruttmann (2011). Using Eqs. (13) and (14), Eq. (12) can be rewritten, as

$$\underline{\mathbf{E}}_p = \begin{bmatrix} \mathbf{A}(\zeta^1, \zeta^2) & \boldsymbol{\Gamma}(\zeta^1, \zeta^2) \end{bmatrix} \begin{Bmatrix} \boldsymbol{\varepsilon}_p(s) \\ \boldsymbol{\alpha}(s) \end{Bmatrix}. \quad (16)$$

Then, from Eq. (10), we obtain the modified total strain energy for beams, as

$$\tilde{U}_{\text{HW}} = \int_0^L \{ \psi(\boldsymbol{\varepsilon}_p, \boldsymbol{\alpha}) + \boldsymbol{\varepsilon}(\mathbf{y}) \cdot \mathbf{r}_p - \boldsymbol{\varepsilon}_p \cdot \mathbf{r}_p - \boldsymbol{\alpha} \cdot \tilde{\mathbf{r}}_p \} ds, \quad (17)$$

where we have defined the strain energy density per unit undeformed length (i.e. line energy density)

$$\psi(\boldsymbol{\varepsilon}_p, \boldsymbol{\alpha}) := \int_{\mathcal{A}} \Psi(\mathbf{E}_p(\boldsymbol{\varepsilon}_p, \boldsymbol{\alpha})) j_0 d\mathcal{A}, \quad (18)$$

and the physical stress resultants

$$\mathbf{r}_p := \int_{\mathcal{A}} \mathbf{A}^T \mathbf{S}_p j_0 d\mathcal{A}, \quad (19)$$

and

$$\tilde{\mathbf{r}}_p := \int_{\mathcal{A}} \boldsymbol{\Gamma}^T \mathbf{S}_p j_0 d\mathcal{A}. \quad (20)$$

The stress resultant field  $\tilde{\mathbf{r}}_p$  is removed from Eq. (17) by assuming that  $\tilde{\mathbf{r}}_p$  is orthogonal to  $\boldsymbol{\alpha}$ , such that the enhanced cross-sectional strain field does not contribute to the internal virtual work (Simo and Rifai, 1990). Therefore, we finally have the following five independent solution fields along the center axis:

- center axis position  $\boldsymbol{\varphi}(s)$ ,
- directors  $\mathbf{d}_\alpha(s)$  ( $\alpha \in \{1, 2\}$ ),
- physical stress resultant  $\mathbf{r}_p(s)$ ,
- physical (kinematic) strain  $\boldsymbol{\varepsilon}_p(s)$ ,
- (physical) enhanced strain  $\boldsymbol{\alpha}(s)$ .

Hereafter, for brevity, we use the notation  $\mathbf{y} := [\boldsymbol{\varphi}, \mathbf{d}_1, \mathbf{d}_2]^T$ . The first variation of the beam strains can be expressed by (Choi et al., 2021, Section A4.2)

$$\delta\boldsymbol{\varepsilon}(\mathbf{y}) = \mathbb{B}_{\text{total}} \delta\mathbf{y}. \quad (21)$$

Taking the first variation of Eq. (17) and substituting Eq. (21) yields

$$G_{\text{int}}^{\text{HW}} \equiv \delta\tilde{U}_{\text{HW}} = \int_0^L \left\{ \begin{array}{c} \delta\mathbf{y} \\ \delta\mathbf{r}_p \\ \delta\boldsymbol{\varepsilon}_p \\ \delta\boldsymbol{\alpha} \end{array} \right\} \cdot \left\{ \begin{array}{c} \mathbb{B}_{\text{total}}^T \mathbf{r}_p \\ \boldsymbol{\varepsilon}(\mathbf{y}) - \boldsymbol{\varepsilon}_p \\ \partial_{\boldsymbol{\varepsilon}_p} \psi(\boldsymbol{\varepsilon}_p, \boldsymbol{\alpha}) - \mathbf{r}_p \\ \partial_{\boldsymbol{\alpha}} \psi(\boldsymbol{\varepsilon}_p, \boldsymbol{\alpha}) \end{array} \right\} ds, \quad (22)$$

where we have defined

$$\partial_{\boldsymbol{\varepsilon}_p} \psi(\boldsymbol{\varepsilon}_p, \boldsymbol{\alpha}) := \int_{\mathcal{A}} \mathbf{A}^T \underline{\partial_{\mathbf{E}_p} \Psi} j_0 d\mathcal{A}, \quad (23)$$

$$\partial_{\boldsymbol{\alpha}} \psi(\boldsymbol{\varepsilon}_p, \boldsymbol{\alpha}) := \int_{\mathcal{A}} \boldsymbol{\Gamma}^T \underline{\partial_{\mathbf{E}_p} \Psi} j_0 d\mathcal{A}, \quad (24)$$

with  $\partial_{\mathbf{E}_p} \Psi := \partial\Psi/\partial\mathbf{E}_p$ . The external virtual work is given by (Choi et al., 2021)

$$G_{\text{ext}}(\delta\mathbf{y}) = \int_0^L \delta\mathbf{y}^T \bar{\mathbf{R}} ds + [\delta\mathbf{y}^T \bar{\mathbf{R}}_0]_{s \in \Gamma_N}, \quad (25)$$



with  $\bar{\mathbf{R}} := [\bar{\mathbf{n}}^T, \bar{\mathbf{m}}^1{}^T, \bar{\mathbf{m}}^2{}^T]^T$  and  $\bar{\mathbf{R}}_0 := [\bar{\mathbf{n}}_0^T, \bar{\mathbf{m}}_0^1{}^T, \bar{\mathbf{m}}_0^2{}^T]^T$ , where  $\bar{\mathbf{n}}$  and  $\bar{\mathbf{m}}^\alpha$  ( $\alpha \in \{1, 2\}$ ) denote the external stress resultants from the external load on the lateral surface of the beam.  $\bar{\mathbf{n}}_0$  and  $\bar{\mathbf{m}}_0^\alpha$  denote the prescribed stress resultants at the boundary  $s \in \Gamma_N$ . Here,  $\Gamma_N \in \emptyset \cup \{0, L\}$  denotes the Neumann boundary, where  $\emptyset$  denotes the empty set. Then, we obtain the following variational equation: Find  $\mathbf{y} \in \mathcal{V}$ ,  $\mathbf{r}_p, \boldsymbol{\varepsilon}_p \in \mathcal{V}_p$ , and  $\boldsymbol{\alpha} \in \mathcal{V}_a$  such that

$$G_{\text{int}}^{\text{HW}}(\mathbf{y}, \mathbf{r}_p, \boldsymbol{\varepsilon}_p, \delta\mathbf{y}, \delta\mathbf{r}_p, \delta\boldsymbol{\varepsilon}_p) = G_{\text{ext}}(\delta\mathbf{y}), \quad \forall \delta\mathbf{y} \in \bar{\mathcal{V}}, \quad \delta\mathbf{r}_p, \delta\boldsymbol{\varepsilon}_p \in \mathcal{V}_p, \quad \text{and } \delta\boldsymbol{\alpha} \in \mathcal{V}_a, \quad (26)$$

with the solution space given by

$$\mathcal{V} := \left\{ \mathbf{y} \in [H^1(0, L)]^d \mid \boldsymbol{\varphi} = \bar{\boldsymbol{\varphi}}_0, \quad \mathbf{d}_1 = \bar{\mathbf{d}}_{10}, \quad \text{and } \mathbf{d}_2 = \bar{\mathbf{d}}_{20} \text{ on } s \in \Gamma_D \right\}, \quad (27)$$

where  $\Gamma_D$  denotes the Dirichlet boundary, such that  $\Gamma_D \cup \Gamma_N = \{0, L\}$  and  $\Gamma_D \cap \Gamma_N = \emptyset$ .  $\bar{\boldsymbol{\varphi}}_0$  and  $\bar{\mathbf{d}}_{\alpha 0}$  ( $\alpha \in \{1, 2\}$ ) denote the prescribed center axis position and director vectors, respectively, and the variational space is given by

$$\bar{\mathcal{V}} := \left\{ \delta\mathbf{y} \in [H^1(0, L)]^d \mid \delta\boldsymbol{\varphi} = \delta\mathbf{d}_1 = \delta\mathbf{d}_2 = \mathbf{0} \text{ on } s \in \Gamma_D \right\}, \quad (28)$$

with  $d = 9$ , which is the number of independent components in  $\mathbf{y}$ . It is chosen such that the physical stress resultants and physical strains belong to  $\mathcal{V}_p := [L^2(0, L)]^{d_p}$ , and the enhanced strain belong to  $\mathcal{V}_a := [L^2(0, L)]^{d_a}$ , where the number of independent functions are  $d_p = 15$ , and  $d_a = 9$ . This means that no inter-element continuity is required for those additional fields, so that we can locally (element-wisely) condense out those corresponding nodal degrees-of-freedom after the finite element approximation. Those condensed coefficients are kept as *internal variables*, which requires additional computer storage. It is noted that we simply follow the conventional treatment to consider the physical stress and strain fields in the open domain  $(0, L) \ni s$ , without any extra boundary conditions, see, e.g. [Wackerfuß and Gruttmann \(2009\)](#). A further investigation on this aspect remains future work.

### 3.2. Linearization

The internal virtual work  $G_{\text{int}}^{\text{HW}}$  of Eq. (22) contains geometrical or material nonlinearities. Therefore, we employ a Newton-Raphson method to solve the variational equation of Eq. (26). An external load is incrementally applied, and using the equilibrium configuration at the previous  $n$ th load step as an initial guess, the solution at the next,  $(n+1)$ th load step is found. The iterative scheme to find the solution is stated as follows: For a given solution  ${}^{n+1}\boldsymbol{\eta}^{(i-1)} := \left\{ {}^{n+1}\mathbf{y}^{(i-1)}, {}^{n+1}\mathbf{r}_p^{(i-1)}, {}^{n+1}\boldsymbol{\varepsilon}_p^{(i-1)}, {}^{n+1}\boldsymbol{\alpha}^{(i-1)} \right\} \in \mathcal{V} \times \mathcal{V}_p \times \mathcal{V}_p \times \mathcal{V}_a$  at the  $(i-1)$ th iteration in the  $(n+1)$ th load step, find the solution increment  $\Delta\boldsymbol{\eta} := \{\Delta\mathbf{y}, \Delta\mathbf{r}_p, \Delta\boldsymbol{\varepsilon}_p, \Delta\boldsymbol{\alpha}\} \in \bar{\mathcal{V}} \times \mathcal{V}_p \times \mathcal{V}_p \times \mathcal{V}_a$  such that

$$\begin{aligned} \Delta G_{\text{int}}^{\text{HW}} \left( {}^{n+1}\boldsymbol{\eta}^{(i-1)}, \delta\boldsymbol{\eta}, \Delta\boldsymbol{\eta} \right) &= G_{\text{ext}}(\delta\mathbf{y}) - G_{\text{int}}^{\text{HW}} \left( {}^{n+1}\boldsymbol{\eta}^{(i-1)}, \delta\boldsymbol{\eta} \right), \\ \forall \delta\mathbf{y} \in \bar{\mathcal{V}}, \quad \delta\mathbf{r}_p, \delta\boldsymbol{\varepsilon}_p \in \mathcal{V}_p, \quad \text{and } \delta\boldsymbol{\alpha} \in \mathcal{V}_a. \end{aligned} \quad (29)$$

The solution is then updated by

$$\left. \begin{aligned} n+1 \mathbf{y}^{(i)} &= n+1 \mathbf{y}^{(i-1)} + \Delta \mathbf{y}, & n+1 \mathbf{y}^{(0)} &= n \mathbf{y}, \\ n+1 \mathbf{r}_p^{(i)} &= n+1 \mathbf{r}_p^{(i-1)} + \Delta \mathbf{r}_p, & n+1 \mathbf{r}_p^{(0)} &= n \mathbf{r}_p, \\ n+1 \boldsymbol{\varepsilon}_p^{(i)} &= n+1 \boldsymbol{\varepsilon}_p^{(i-1)} + \Delta \boldsymbol{\varepsilon}_p, & n+1 \boldsymbol{\varepsilon}_p^{(0)} &= n \boldsymbol{\varepsilon}_p, \\ n+1 \boldsymbol{\alpha}^{(i)} &= n+1 \boldsymbol{\alpha}^{(i-1)} + \Delta \boldsymbol{\alpha}, & n+1 \boldsymbol{\alpha}^{(0)} &= n \boldsymbol{\alpha}, \end{aligned} \right\} \quad (30)$$

where the initial guess is given by the converged solution in the previous ( $n$ th) load step. We obtain the increment of the internal virtual work  $\Delta G_{\text{int}}^{\text{HW}}$  by taking the directional derivative of Eq. (22), as

$$\Delta G_{\text{int}}^{\text{HW}} = \int_0^L \begin{Bmatrix} \delta \mathbf{y} \\ \delta \mathbf{r}_p \\ \delta \boldsymbol{\varepsilon}_p \\ \delta \boldsymbol{\alpha} \end{Bmatrix}^T \begin{bmatrix} \mathbf{Y}^T \mathbf{k}_G \mathbf{Y} & \mathbb{B}_{\text{total}}^T & \mathbf{0}_{9 \times 15} & \mathbf{0}_{9 \times n_a} \\ & \mathbf{0}_{15 \times 15} & -\mathbf{1}_{15 \times 15} & \mathbf{0}_{15 \times n_a} \\ & & \mathbb{C}_p & \mathbb{C}_p^{\text{aeT}} \\ \text{sym.} & & & \mathbb{C}_p^{\text{aa}} \end{bmatrix} \begin{Bmatrix} \Delta \mathbf{y} \\ \Delta \mathbf{r}_p \\ \Delta \boldsymbol{\varepsilon}_p \\ \Delta \boldsymbol{\alpha} \end{Bmatrix} ds, \quad (31)$$

with the operator (Choi et al., 2021, Section A.4.4)

$$\mathbf{Y} := \begin{bmatrix} (\bullet)_{,s} \mathbf{1}_{3 \times 3} & \mathbf{0}_{3 \times 3} & \mathbf{0}_{3 \times 3} \\ \mathbf{0}_{3 \times 3} & (\bullet)_{,s} \mathbf{1}_{3 \times 3} & \mathbf{0}_{3 \times 3} \\ \mathbf{0}_{3 \times 3} & \mathbf{0}_{3 \times 3} & (\bullet)_{,s} \mathbf{1}_{3 \times 3} \\ \mathbf{0}_{3 \times 3} & \mathbf{1}_{3 \times 3} & \mathbf{0}_{3 \times 3} \\ \mathbf{0}_{3 \times 3} & \mathbf{0}_{3 \times 3} & \mathbf{1}_{3 \times 3} \end{bmatrix}_{15 \times 9}. \quad (32)$$

Here we have defined the constitutive matrices

$$\mathbb{C}_p := \int_{\mathcal{A}} \mathbf{A}^T \underline{\underline{\mathbf{C}_p}} \mathbf{A} j_0 d\mathcal{A}, \quad (33)$$

$$\mathbb{C}_p^{\text{aa}} := \int_{\mathcal{A}} \boldsymbol{\Gamma}^T \underline{\underline{\mathbf{C}_p}} \boldsymbol{\Gamma} j_0 d\mathcal{A}, \quad (34)$$

$$\mathbb{C}_p^{\text{ae}} := \int_{\mathcal{A}} \boldsymbol{\Gamma}^T \underline{\underline{\mathbf{C}_p}} \mathbf{A} j_0 d\mathcal{A}, \quad (35)$$

where

$$\underline{\underline{\mathbf{C}_p}} := \frac{\partial^2 \Psi}{\partial \mathbf{E}_p \partial \mathbf{E}_p}, \quad (36)$$

and  $\underline{\underline{(\bullet)}}$  denotes the Voigt notation of a fourth-order tensor.

## 4. An isogeometric finite element discretization

### 4.1. NURBS curve: An exact representation of the initial geometry

The initial geometry of the beam's center axis can be represented by a spline curve. In the framework of IGA, we utilize the same spline basis functions utilized in the CAD model. Here we summarize the construction of NURBS curves. More detailed explanation on the properties of NURBS, and algorithms for the knot insertion and degree elevation can be found in Piegl and Tiller (1996). Those two operations are not commutative. The knot insertion followed by a degree elevation maintains the maximum

continuity of the original curve, which is so called  $k$ -refinement. The other way around, increasing the degree of each curve segment after the knot insertion, corresponds to the classical  $p$ -refinement. For a specific example of these mesh refinement processes, see [Hughes et al. \(2005\)](#). For a given patch of a NURBS curve, we have the knot vector  $\tilde{\Xi} = \{\xi_1, \xi_2, \dots, \xi_{n_{cp}+p+1}\}$ , where  $\xi_i \in \mathbb{R}$  is the  $i$ th knot,  $p$  is the degree of basis functions, and  $n_{cp}$  is the total number of basis functions (or control points). B-spline basis functions are recursively defined ([Piegl and Tiller, 1996](#)). For  $p = 0$ , they are defined by

$$B_I^0(\xi) = \begin{cases} 1 & \text{if } \xi_I \leq \xi < \xi_{I+1}, \\ 0 & \text{otherwise,} \end{cases} \quad (37)$$

and for  $p = 1, 2, 3, \dots$ , they are defined by

$$B_I^p(\xi) = \frac{\xi - \xi_I}{\xi_{I+p} - \xi_I} B_I^{p-1}(\xi) + \frac{\xi_{I+p+1} - \xi}{\xi_{I+p+1} - \xi_{I+1}} B_{I+1}^{p-1}(\xi), \quad (38)$$

where  $\xi \in \Xi \subset \mathbb{R}$  denotes the parametric coordinate, and  $\Xi := [\xi_1, \xi_{n_{cp}+p+1}]$  represents the parametric domain. We employ NURBS to exactly represent the initial geometries from a conic section like circle and ellipse. From the B-spline basis functions, the NURBS basis functions are defined by

$$N_I^p(\xi) = \frac{B_I^p(\xi) w_I}{\sum_{J=1}^{n_{cp}} B_J^p(\xi) w_J}, \quad (39)$$

where  $w_I$  denotes the given weight of the  $I$ th control point. If the weights are equal, the NURBS becomes a B-spline. The geometry of the beam's initial center axis can be represented by a NURBS curve, as

$$\mathbf{X}(\xi) = \sum_{I=1}^{n_{cp}} N_I^p(\xi) \mathbf{X}_I, \quad (40)$$

where  $\mathbf{X}_I$  are the control point positions. The arc-length parameter along the initial center axis can be expressed by the mapping  $s(\xi) : \Xi \rightarrow [0, L]$ , defined by

$$s(\xi) := \int_{\xi_1}^{\eta=\xi} \|\mathbf{X}_{,\eta}(\eta)\| d\eta. \quad (41)$$

Then the Jacobian of the mapping is derived as

$$\tilde{j} := \frac{ds}{d\xi} = \|\mathbf{X}_{,\xi}(\xi)\|. \quad (42)$$

In the discretization of the variational form, we often use the notation  $N_{I,s}^p$  for brevity, which is defined by

$$N_{I,s}^p := N_{I,\xi}^p \frac{d\xi}{ds} = \frac{1}{\tilde{j}} N_{I,\xi}^p, \quad (43)$$

where  $N_{I,\xi}^p$  denotes the differentiation of the basis function  $N_I^p(\xi)$  with respect to  $\xi$ .

#### 4.2. Discretization of the variational form

We may choose different degrees of basis functions for the displacements of the center axis, and directors, which are denoted by  $p$  and  $p_d$ , respectively. In this paper, we propose to use  $p_d = p - 1$  for

the field consistency in the finite element approximation of the transverse shear strain of Eq. (7c). In the entire domain of a curve patch, we have the approximated current center axis position

$$\boldsymbol{\varphi}^h(s(\xi)) = \sum_{I=1}^{n_{\text{cp}}} N_I^p(\xi) \boldsymbol{\varphi}_{\alpha I}, \quad \xi \in \Xi, \quad (44)$$

and total director displacement  $\bar{\mathbf{d}}_\alpha := \mathbf{d}_\alpha - \mathbf{D}_\alpha$  ( $\alpha \in \{1, 2\}$ )

$$\bar{\mathbf{d}}_\alpha^h(s(\xi)) = \sum_{J=1}^{n_{\text{cp}}^d} N_J^{p_d}(\xi) \bar{\mathbf{d}}_{\alpha J}, \quad \alpha \in \{1, 2\}, \quad \xi \in \Xi, \quad (45)$$

where  $n_{\text{cp}}^d$  denotes the total number of control coefficients for the director displacement field in the patch. In IGA, we define an element by a half-open interval between two distinct knots, i.e. a non-zero knot span. Let  $\Xi_e := [\xi_1^e, \xi_2^e] \ni \xi$  denote the  $e$ th element, such that  $\Xi = \Xi_1 \cup \Xi_2 \cup \dots \cup \Xi_{n_{\text{el}}}$ , where  $n_{\text{el}}$  denotes the total number of elements. For the last element of an open curve (i.e.  $e = n_{\text{el}}$ ), we consider a closed interval  $\Xi_{n_{\text{el}}} := [\xi_1^{n_{\text{el}}}, \xi_2^{n_{\text{el}}}]$  to include the end point. We use the same number of elements for both displacement fields of the axis, and directors. We have  $n_e = p + 1$ , and  $n_e^d = p_d + 1$  local support basis functions in every element, for the axis and director displacement fields, respectively. Then, we can rewrite Eqs. (44) and (45) in each element, as

$$\boldsymbol{\varphi}^h(s(\xi)) = \sum_{I=1}^{n_e} N_I^p(\xi) \boldsymbol{\varphi}_I^e, \quad \xi \in \Xi_e. \quad (46)$$

and

$$\bar{\mathbf{d}}_\alpha^h(s(\xi)) = \sum_{I=1}^{n_e^d} N_I^{p_d}(\xi) \bar{\mathbf{d}}_{\alpha I}^e, \quad \xi \in \Xi_e. \quad (47)$$

Combining Eqs. (46) and (47), we obtain

$$\mathbf{y}^h = \left\{ \begin{array}{c} \boldsymbol{\varphi}^h \\ \bar{\mathbf{d}}_1^h \\ \bar{\mathbf{d}}_2^h \end{array} \right\} = \mathbb{N}_e(\xi) \mathbf{y}^e, \quad \xi \in \Xi_e, \quad (48)$$

with

$$\mathbb{N}_e := \left[ \begin{array}{ccc|ccc} N_1^p \mathbf{1}_{3 \times 3} & \cdots & N_{n_e}^p \mathbf{1}_{3 \times 3} & \mathbf{0}_{3 \times 6n_e^d} & & \\ & \mathbf{0}_{6 \times 3n_e} & & N_1^{p_d} \mathbf{1}_{6 \times 6} & \cdots & N_{n_e^d}^{p_d} \mathbf{1}_{6 \times 6} \end{array} \right], \quad (49)$$

and  $\mathbf{y}^e := [\boldsymbol{\varphi}_1^{eT}, \dots, \boldsymbol{\varphi}_{n_e}^{eT}, \bar{\mathbf{d}}_1^{eT}, \dots, \bar{\mathbf{d}}_{n_e^d}^{eT}]^T$ , where  $\boldsymbol{\varphi}_I \in \mathbb{R}^3$ , and  $\bar{\mathbf{d}}_J := [\bar{\mathbf{d}}_{1J}^T, \bar{\mathbf{d}}_{2J}^T]^T \in \mathbb{R}^6$  denote the control coefficient vectors for the current axis position, and the total displacement of directors, respectively.

In the approximation of physical stress resultants, and strains, we allow for inter-element discontinuity for an element-wise static condensation process, and use Lagrange interpolation functions. We first define a mapping from a parametric domain  $[-1, 1] \ni \bar{\xi}$ , where the Lagrange functions are defined, to the closed interval  $\Xi_e := [\xi_1^e, \xi_2^e] \ni \xi$ , as

$$\bar{\xi} = 1 - 2 \left( \frac{\xi_2^e - \xi}{\xi_2^e - \xi_1^e} \right). \quad (50)$$

The physical stress resultants are approximated, using the Lagrange polynomial functions of degree  $p_p$ , as

$$\mathbf{r}_p^h(s(\xi)) = \left[ L_1^{p_p}(\bar{\xi}) \mathbf{1}_{15 \times 15} \quad \cdots \quad L_{n_e^p}^{p_p}(\bar{\xi}) \mathbf{1}_{15 \times 15} \right] \left\{ \begin{array}{c} \mathbf{r}_1^e \\ \vdots \\ \mathbf{r}_{n_e^p}^e \end{array} \right\} =: \mathbb{L}_e^{p_p}(\bar{\xi}) \mathbf{r}^e, \quad \bar{\xi} \in [-1, 1], \quad (51)$$

where  $\mathbf{r}_I^e \in \mathbb{R}^{15}$  denotes the coefficient array for the physical stress resultants.  $L_i^{p_p}$  denotes the  $i$ th Lagrange polynomial functions of degree  $p_p$  in each element, and  $n_e^p = p_p + 1$  denotes the number of basis functions in  $e$ th element. Similarly, the physical beam strains are approximated by

$$\boldsymbol{\varepsilon}_p^h(\xi(\bar{\xi})) = \mathbb{L}_e^{p_p}(\bar{\xi}) \mathbf{e}^e, \text{ with } \mathbf{e}^e := \begin{Bmatrix} \mathbf{e}_1^e \\ \vdots \\ \mathbf{e}_{n_e^p}^e \end{Bmatrix}, \bar{\xi} \in [-1, 1], \quad (52)$$

where  $\mathbf{e}_I \in \mathbb{R}^{15}$  denotes the coefficient vector for the physical beam strains,  $I \in \{1, 2, \dots, n_e^p\}$ , and  $n_e^p = p_p + 1$  denotes the number of basis functions for the approximation of physical beam strains within the element. The physical enhanced strain parameters are approximated by linear Lagrange polynomial bases within each element (i.e.  $p_a = 1$ ), as (Choi et al., 2021)

$$\boldsymbol{\alpha}^h(\tilde{\xi}) = \begin{bmatrix} L_1^{p_a}(\tilde{\xi}) \mathbf{1}_{9 \times 9} & L_2^{p_a}(\tilde{\xi}) \mathbf{1}_{9 \times 9} \end{bmatrix} \begin{Bmatrix} \boldsymbol{\alpha}_1^e \\ \boldsymbol{\alpha}_2^e \end{Bmatrix} =: \mathbb{L}_e^{p_a}(\tilde{\xi}) \boldsymbol{\alpha}^e, \quad (53)$$

where  $\boldsymbol{\alpha}^e$  are the nodal vectors of the enhanced strain parameters. Substituting Eq. (52) into Eq. (22), the internal virtual work is approximated by

$$G_{\text{int}}^{\text{HW}} \approx \sum_{e=1}^{n_{\text{el}}} \int_{\Xi_e} \begin{Bmatrix} \delta \mathbf{y}^e \\ \delta \mathbf{r}^e \\ \delta \mathbf{e}^e \\ \delta \boldsymbol{\alpha}^e \end{Bmatrix} \cdot \mathbf{F}_{\text{int}}^e \tilde{j} \, d\xi = \delta \mathbf{y}^{*\text{T}} \left( \mathbf{A}_{e=1}^{n_{\text{el}}} \mathbf{F}_{\text{int}}^e \right), \quad (54)$$

with the elemental internal load vector,  $\mathbf{F}_{\text{int}}^e := [\mathbf{f}_y^{e\text{T}}, \mathbf{f}_r^{e\text{T}}, \mathbf{f}_\varepsilon^{e\text{T}}, \mathbf{f}_a^{e\text{T}}]^\text{T}$ , defined by

$$[\mathbf{f}_y^e]_{9n_e \times 1} := \int_{\Xi_e} \mathbb{B}_{\text{total}}^{e\text{T}} \mathbf{r}_p^h \tilde{j} \, d\xi, \quad (55a)$$

$$[\mathbf{f}_r^e]_{15n_e \times 1} := \int_{\Xi_e} \mathbb{L}_e^\text{T} \{ \boldsymbol{\varepsilon}(\mathbf{y}^h) - \boldsymbol{\varepsilon}_p^h \} \tilde{j} \, d\xi, \quad (55b)$$

$$[\mathbf{f}_\varepsilon^e]_{15n_e \times 1} := \int_{\Xi_e} \mathbb{L}_e^\text{T} \{ \partial_{\boldsymbol{\varepsilon}_p} \psi(\boldsymbol{\varepsilon}_p^h, \boldsymbol{\alpha}^h) - \mathbf{r}_p^h \} \tilde{j} \, d\xi, \quad (55c)$$

$$[\mathbf{f}_a^e]_{15n_e \times 1} := \int_{\Xi_e} \mathbb{L}_e^\text{T} \partial_{\boldsymbol{\alpha}} \psi(\boldsymbol{\varepsilon}_p^h, \boldsymbol{\alpha}^h) \tilde{j} \, d\xi. \quad (55d)$$

$\mathbf{A}$  denotes the finite element assembly operator, and  $\mathbf{y}^*$  denotes the global array of the coefficients in the center axis position, director displacement, and the additional stress and strain fields. Similarly, the increment of internal virtual work is also approximated by

$$\Delta G_{\text{int}}^{\text{HW}} \approx \sum_{e=1}^{n_{\text{el}}} \begin{Bmatrix} \delta \mathbf{y}^e \\ \delta \mathbf{r}^e \\ \delta \mathbf{e}^e \\ \delta \boldsymbol{\alpha}^e \end{Bmatrix} \cdot \mathbf{K}_{\text{int}}^e \begin{Bmatrix} \Delta \mathbf{y}^e \\ \Delta \mathbf{r}^e \\ \Delta \mathbf{e}^e \\ \Delta \boldsymbol{\alpha}^e \end{Bmatrix} = \delta \mathbf{y}^{*\text{T}} \left( \mathbf{A}_{e=1}^{n_{\text{el}}} \mathbf{K}_{\text{int}}^e \right) \Delta \mathbf{y}^*, \quad (56)$$

and the element tangent stiffness matrix

$$\mathbf{K}_{\text{int}}^e := \begin{bmatrix} \mathbf{k}_{yy}^e & \mathbf{k}_{ry}^{e\text{T}} & \mathbf{0}_{dn_e \times d_p n_e^p} & \mathbf{0}_{dn_e \times d_a n_e^a} \\ & \mathbf{0}_{d_p n_e^p \times d_p n_e^p} & \mathbf{k}_{r\varepsilon}^e & \mathbf{0}_{d_p n_e^p \times d_a n_e^a} \\ & & \mathbf{k}_{\varepsilon\varepsilon}^e & \mathbf{k}_{a\varepsilon}^{e\text{T}} \\ \text{sym.} & & & \mathbf{k}_{aa}^e \end{bmatrix}, \quad (57)$$

with

$$\mathbf{k}_{yy}^e := \int_{\Xi_e} \mathbb{Y}_e^{\text{T}} \mathbf{k}_G \mathbb{Y}_e \tilde{j} \, d\xi, \quad (58a)$$

$$\mathbf{k}_{ry}^e := \int_{\Xi_e} \mathbb{L}_e^{\text{T}} \mathbb{B}_{\text{total}}^e \tilde{j} \, d\xi, \quad (58b)$$

$$\mathbf{k}_{r\varepsilon}^e := - \int_{\Xi_e} \mathbb{L}_e^{\text{T}} \mathbb{L}_e \tilde{j} \, d\xi, \quad (58c)$$

$$\mathbf{k}_{\varepsilon\varepsilon}^e := \int_{\Xi_e} \mathbb{L}_e^{\text{T}} \mathbb{C}_p \mathbb{L}_e \tilde{j} \, d\xi, \quad (58d)$$

$$\mathbf{k}_{a\varepsilon}^e := \int_{\Xi_e} \mathbb{L}_e^{\text{T}} \mathbb{C}_p^{a\varepsilon} \mathbb{L}_e \tilde{j} \, d\xi, \quad (58e)$$

$$\mathbf{k}_{aa}^e := \int_{\Xi_e} \mathbb{L}_e^{\text{T}} \mathbb{C}_p^{aa} \mathbb{L}_e \tilde{j} \, d\xi. \quad (58f)$$

Detailed expressions of  $\mathbf{k}_G$  and  $\mathbb{Y}_e$  can be found in Appendix A.1. The external virtual work of Eq. (25) is also approximated by

$$G_{\text{ext}}(\delta \mathbf{y}) \approx \delta \mathbf{y}^{\text{T}} \mathbf{F}_{\text{ext}}, \quad \text{with } \mathbf{F}_{\text{ext}} := \sum_{e=1}^{n_{\text{el}}} \mathbf{F}_{\text{ext}}^e + \mathbf{A} [\bar{\mathbf{R}}_0]_{s \in \Gamma_N}, \quad (59)$$

where  $\mathbf{y}$  denotes the global array of the control coefficients for the center axis position, and director displacement field. We have also defined

$$\mathbf{F}_{\text{ext}}^e := \int_{\Xi_e} \mathbb{N}_e^{\text{T}} \bar{\mathbf{R}} \tilde{j} \, d\xi. \quad (60)$$

Substituting Eqs. (54) and (56) into Eq. (29) gives

$$\delta \mathbf{y}^{*\text{T}} \left( \sum_{e=1}^{n_{\text{el}}} \mathbf{A} \mathbf{K}_{\text{int}}^e \right) \Delta \mathbf{y}^* = \delta \mathbf{y}^{\text{T}} \mathbf{F}_{\text{ext}} - \delta \mathbf{y}^{*\text{T}} \left( \sum_{e=1}^{n_{\text{el}}} \mathbf{A} \mathbf{F}_{\text{int}}^e \right). \quad (61)$$

#### 4.2.1. Element-wise static condensation

Since the physical strain and stress resultants may have discontinuities between adjacent elements, Eq. (61) can be rewritten as

$$\sum_{e=1}^{n_{\text{el}}} \delta \mathbf{y}^{e\text{T}} (\mathbf{k}_{yy}^e \Delta \mathbf{y}^e + \mathbf{k}_{ry}^{e\text{T}} \Delta \mathbf{r}^e) = \delta \mathbf{y}^{\text{T}} \mathbf{F}_{\text{ext}} - \sum_{e=1}^{n_{\text{el}}} \delta \mathbf{y}^{e\text{T}} \mathbf{f}_y^e, \quad (62a)$$

$$\mathbf{k}_{ry}^{e\text{T}} \Delta \mathbf{y}^e + \mathbf{k}_{r\varepsilon}^e \Delta \mathbf{e}^e = -\mathbf{f}_r^e, \quad e \in \{1, \dots, n_{\text{el}}\}, \quad (62b)$$

$$\mathbf{k}_{r\varepsilon}^{e\text{T}} \Delta \mathbf{r}^e + \mathbf{k}_{\varepsilon\varepsilon}^e \Delta \mathbf{e}^e + \mathbf{k}_{a\varepsilon}^{e\text{T}} \Delta \alpha^e = -\mathbf{f}_\varepsilon^e, \quad e \in \{1, \dots, n_{\text{el}}\}, \quad (62c)$$

$$\mathbf{k}_{a\varepsilon}^e \Delta \mathbf{e}^e + \mathbf{k}_{aa}^e \Delta \alpha^e = -\mathbf{f}_a^e, \quad e \in \{1, \dots, n_{\text{el}}\}. \quad (62d)$$

Since, the matrices  $\mathbf{k}_{r\varepsilon}^e$  and  $\mathbf{k}_{aa}^e$  are invertible, we obtain from Eqs. (62b)-(62d)

$$\Delta \mathbf{e}^e = -\mathbf{k}_{r\varepsilon}^{e-1} (\mathbf{f}_r^e + \mathbf{k}_{ry}^e \Delta \mathbf{y}^e), \quad (63a)$$

$$\Delta \boldsymbol{\alpha}^e = -\mathbf{k}_{aa}^{e-1} (\mathbf{f}_a^e + \mathbf{k}_{a\varepsilon}^e \Delta \mathbf{e}^e), \quad (63b)$$

$$\Delta \mathbf{r}^e = -\mathbf{k}_{r\varepsilon}^{e-T} (\mathbf{f}_\varepsilon^e + \mathbf{k}_{\varepsilon\varepsilon}^e \Delta \mathbf{e}^e + \mathbf{k}_{a\varepsilon}^{eT} \Delta \boldsymbol{\alpha}^e). \quad (63c)$$

Then, Eq. (62a) can be rewritten as

$$\delta \mathbf{y}^T \bar{\mathbf{K}} \Delta \mathbf{y} = \delta \mathbf{y}^T \bar{\mathbf{F}}, \quad (64)$$

where we define

$$\bar{\mathbf{K}} := \mathbf{A} \sum_{e=1}^{n_{el}} \bar{\mathbf{K}}_{\text{int}}^e, \quad (65)$$

and

$$\bar{\mathbf{F}} := \mathbf{A} \sum_{e=1}^{n_{el}} (\mathbf{F}_{\text{ext}}^e - \bar{\mathbf{F}}_{\text{int}}^e) + \mathbf{A} [\bar{\mathbf{R}}_0]_{s \in \Gamma_N}, \quad (66)$$

with

$$\bar{\mathbf{K}}_{\text{int}}^e := \mathbf{k}_{yy}^e + \mathbf{k}_{ry}^{eT} \mathbf{k}_{r\varepsilon}^{e-T} (\mathbf{k}_{\varepsilon\varepsilon}^e - \mathbf{k}_{a\varepsilon}^{eT} \mathbf{k}_{aa}^{e-1} \mathbf{k}_{a\varepsilon}^e) \mathbf{k}_{r\varepsilon}^{e-1} \mathbf{k}_{ry}^e, \quad (67)$$

and

$$\bar{\mathbf{F}}_{\text{int}}^e := \mathbf{f}_y^e - \mathbf{k}_{ry}^{eT} \mathbf{k}_{r\varepsilon}^{e-T} \{ \mathbf{f}_\varepsilon^e - \mathbf{k}_{\varepsilon\varepsilon}^e \mathbf{k}_{r\varepsilon}^{e-1} \mathbf{f}_r^e - \mathbf{k}_{a\varepsilon}^{eT} \mathbf{k}_{aa}^{e-1} (\mathbf{f}_a^e - \mathbf{k}_{a\varepsilon}^e \mathbf{k}_{r\varepsilon}^{e-1} \mathbf{f}_r^e) \}. \quad (68)$$

The only matrices which need to be inverted are  $\mathbf{k}_{r\varepsilon}^e$  and  $\mathbf{k}_{aa}^e$ . By applying the homogeneous displacement boundary conditions, we finally have the following reduced system of linear equations at  $i$ th iteration in the  $(n+1)$ th load step

$${}^{n+1} \bar{\mathbf{K}}_r^{(i-1)} \Delta \mathbf{y}_r = {}^{n+1} \bar{\mathbf{F}}_r^{(i-1)}, \quad (69)$$

where  $(\bullet)_r$  denotes the reduced vector or matrix.

#### 4.2.2. Update of the configuration and internal variables

Using the solution increment  $\Delta \mathbf{y}_r$  obtained by solving Eq. (69), we update the control coefficients  $\boldsymbol{\varphi}_I$  and  $\bar{\mathbf{d}}_J$  by the following procedure: At the  $i$ th iteration in the  $(n+1)$ th load step, we update

$${}^{n+1} \boldsymbol{\varphi}_I^{(i)} = {}^{n+1} \boldsymbol{\varphi}_I^{(i-1)} + \Delta \boldsymbol{\varphi}_I^{(i)}, \quad I \in \{1, 2, \dots, n_{cp}\}, \quad (70a)$$

$${}^{n+1} \bar{\mathbf{d}}_J^{(i)} = {}^{n+1} \bar{\mathbf{d}}_J^{(i-1)} + \Delta \bar{\mathbf{d}}_J^{(i)}, \quad J \in \{1, 2, \dots, n_{cp}^d\}, \quad (70b)$$

with the initial guesses  ${}^{n+1} \boldsymbol{\varphi}_I^{(0)} \equiv {}^n \boldsymbol{\varphi}_I$ , and  ${}^{n+1} \bar{\mathbf{d}}_J^{(0)} \equiv {}^n \bar{\mathbf{d}}_J$ , from the equilibrium configuration in the previous ( $n$ th) load step. Further, from  $\Delta \mathbf{y}_r$ ,  $\Delta \mathbf{y}^e$  can be simply extracted for each element, and is substituted into Eq. (63) to obtain the increment of internal variables  $\Delta \mathbf{e}^e$ ,  $\Delta \mathbf{r}^e$ , and  $\Delta \boldsymbol{\alpha}^e$ . Then, for every element  $e \in \{1, \dots, n_{el}\}$ , we update

$${}^{n+1} \mathbf{e}^e(i) = {}^{n+1} \mathbf{e}^e(i-1) + \Delta \mathbf{e}^e, \quad (71a)$$

$${}^{n+1} \mathbf{r}^e(i) = {}^{n+1} \mathbf{r}^e(i-1) + \Delta \mathbf{r}^e, \quad (71b)$$

$${}^{n+1} \boldsymbol{\alpha}^e(i) = {}^{n+1} \boldsymbol{\alpha}^e(i-1) + \Delta \boldsymbol{\alpha}^e, \quad (71c)$$

with the initial guesses  ${}^{n+1} \mathbf{e}^e(0) \equiv {}^n \mathbf{e}^e$ ,  ${}^{n+1} \mathbf{r}^e(0) \equiv {}^n \mathbf{r}^e$ , and  ${}^{n+1} \boldsymbol{\alpha}^e(0) \equiv {}^n \boldsymbol{\alpha}^e$ , from the converged solution in the previous ( $n$ th) load step.

## 5. Imposition of rotational continuity between beams

In order to facilitate the connection of multiple beams with an arbitrary initial intersection angle and rotational continuity, we introduce rotational degrees-of-freedom for directors at the ends of beam. Here we are only concerned with the rigid joint condition, that is, all the connected beams' cross-sections may have only three-rotational degrees-of-freedom. However, in contrast to the conventional rigid joint, our formulation may still allow stretching along the two directors in each cross-section. The presented formulation is limited to the finite element basis functions having Kronecker-delta property at the end points of the beam. Therefore, for IGA, we only use clamped knot vectors, so that the NURBS basis functions have Kronecker-delta property at the end points of the beam. This enables us to simply consider only the director coefficients corresponding to the end points, as in the conventional finite element formulation, e.g., see [Romero and Armero \(2002\)](#).

### 5.1. Multiplicative decomposition of the directors

The director vectors can be decomposed into a unit director and a scalar stretch, as

$$\mathbf{d}_\alpha(s) = \lambda_\alpha(s) \mathbf{t}_\alpha(s), \quad (72)$$

with the stretch  $\lambda_\alpha(s) := \|\mathbf{d}_\alpha(s)\| > 0$ , where no summation is implied on  $\alpha \in \{1, 2\}$ . Further, the unit vectors can be expressed by rotational transformation as

$$\mathbf{t}_\alpha(s) = \mathbf{\Lambda}_\alpha(s) \mathbf{E}_\alpha \text{ with } \mathbf{\Lambda}_\alpha(s) \in \mathbb{S}_\alpha^2, \alpha \in \{1, 2\}, \quad (73)$$

where we define ([Simo and Fox, 1989](#))

$$\mathbb{S}_\alpha^2 := \{ \mathbf{\Lambda} \in \text{SO}(3) \mid \mathbf{\Lambda} \boldsymbol{\psi} = \boldsymbol{\psi}, \text{ and } \boldsymbol{\psi} \in \mathbb{R}^3 \text{ satisfies } \boldsymbol{\psi} \cdot \mathbf{E}_\alpha = 0 \}. \quad (74)$$

$\text{SO}(3)$  defines the set of proper orthogonal tensors in three-dimensional space, and  $\mathbb{S}_\alpha^2$  is a subset of  $\text{SO}(3)$  such that the axis of rotation is orthogonal to  $\mathbf{E}_\alpha \in \mathbb{R}^3$ . At an admissible perturbed configuration, Eq. (73) can be rewritten as

$$\mathbf{t}_{\alpha\varepsilon}(s) = \mathbf{\Lambda}_{\alpha\varepsilon}(s) \mathbf{E}_\alpha, \varepsilon \in \mathbb{R}, \quad (75)$$

where the subscript  $(\bullet)_\varepsilon$  indicates the dependence of  $(\bullet)$  to the perturbation amount  $\varepsilon$ . Hereafter, we often omit the argument  $s$  for brevity. Taking the directional derivative of Eq. (75) yields

$$\delta \mathbf{t}_\alpha := \frac{d}{d\varepsilon} \mathbf{t}_{\alpha\varepsilon} \Big|_{\varepsilon=0} = \widehat{\delta \boldsymbol{\theta}_\alpha} \mathbf{t}_\alpha, \alpha \in \{1, 2\}, \quad (76)$$

where  $\widehat{\delta \boldsymbol{\theta}_\alpha} := \delta \mathbf{\Lambda}_\alpha \mathbf{\Lambda}_\alpha^T$  (without summation on  $\alpha$ ) is a skew-symmetric tensor, so that we have

$$\delta \mathbf{t}_\alpha = \delta \boldsymbol{\theta}_\alpha \times \mathbf{t}_\alpha, \alpha \in \{1, 2\}. \quad (77)$$

We use the notation  $\widehat{(\bullet)}$  to represent the skew-symmetric tensor associated with a given vector  $(\bullet) \in \mathbb{R}^3$ , such that  $\widehat{(\bullet)} \mathbf{h} = (\bullet) \times \mathbf{h}, \forall \mathbf{h} \in \mathbb{R}^3$ . Note that  $\delta \boldsymbol{\theta}_\alpha$  is constrained by the condition,  $\delta \boldsymbol{\theta}_\alpha \cdot \mathbf{t}_\alpha = 0$  (no sum on  $\alpha \in \{1, 2\}$ ) ([Simo and Fox, 1989](#)). Thus, each unit director has only two rotational DOFs. Here, for simplicity, we restrict our discussion by the further constraint

$$\delta \boldsymbol{\theta}_1 = \delta \boldsymbol{\theta}_2 \equiv \delta \boldsymbol{\theta}. \quad (78)$$



Thus, we eventually have three-rotational DOFs of the cross-section at a selected end point. Note that the stretches along the directors,  $\lambda_\alpha$  ( $\alpha \in \{1, 2\}$ ) are kinematically not constrained. Then, substituting Eq. (78) into Eq. (77), we have

$$\delta \mathbf{t}_\alpha = \delta \boldsymbol{\theta} \times \mathbf{t}_\alpha, \quad \alpha \in \{1, 2\}. \quad (79)$$

Then, the orthogonal tensor  $\mathbf{\Lambda}_{\alpha\varepsilon}$  at the perturbed configuration can be expressed using an exponential map by (Simo and Vu-Quoc, 1986)

$$\mathbf{\Lambda}_{\alpha\varepsilon} = \exp \left[ \varepsilon \widehat{\delta \boldsymbol{\theta}} \right] \mathbf{\Lambda}_\alpha, \quad \varepsilon \in \mathbb{R}, \quad \alpha \in \{1, 2\}. \quad (80)$$

Taking the first variation of the director in Eq. (72), and substituting Eq. (79) gives

$$\begin{Bmatrix} \delta \mathbf{d}_1 \\ \delta \mathbf{d}_2 \end{Bmatrix} = \mathbf{\Xi} \begin{Bmatrix} \delta \boldsymbol{\theta} \\ \delta \mu_1 \\ \delta \mu_2 \end{Bmatrix}, \quad (81)$$

where  $\mu_\alpha := \ln \lambda_\alpha / \lambda_\alpha$  (no sum on  $\alpha \in \{1, 2\}$ ) defines the logarithmic stretch ratio, and we also define the operator,

$$\mathbf{\Xi} := \begin{bmatrix} -\widehat{\mathbf{d}}_1 & \mathbf{d}_1 & \mathbf{0}^T \\ -\widehat{\mathbf{d}}_2 & \mathbf{0}^T & \mathbf{d}_2 \end{bmatrix}. \quad (82)$$

## 5.2. Isogeometric finite element formulation

Fig. 3 illustrates two cases of junction positions in a curve patch, where we can apply the joint condition to

- Case 1 (joint at the left-end): the first control point ( $K = 1$ ) having local support at the first element  $e = 1$ , or
- Case 2 (joint at the right-end): the last control point ( $K = n_{\text{cp}}^{\text{d}}$ ) having local support at the last element  $n_{\text{el}}$ ,

where  $K$  denotes the index of control points in a given curve patch. Here, for simplicity, we consider that an end element has a joint condition only at one end.

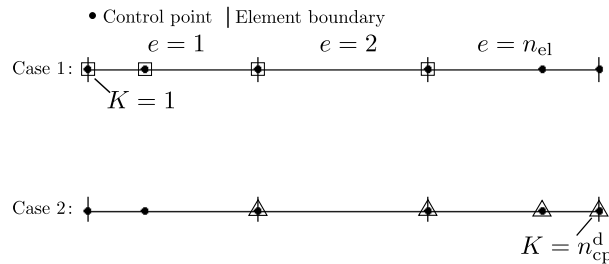


Figure 3: Illustration of two cases of joint positions. The curve patch (solid line) of  $p_{\text{d}} = 3$  consists of three elements, and  $\square$  and  $\triangle$  indicate the control points having local support at the first ( $e = 1$ ) and the last element ( $e = n_{\text{el}}$ ) of the patch, respectively. A joint condition can be imposed at the left end (the first control point, i.e.  $K = 1$ ) of the first element (top figure) or the right end (last control point, i.e.  $K = n_{\text{cp}}^{\text{d}}$ ) (bottom figure).

We also denote a set of indices of elements having a joint condition by  $\mathcal{J}$ . That is, if  $e$ th element has a joint condition,  $e \in \mathcal{J}$ , otherwise,  $e \notin \mathcal{J}$ . At the end control point of the patch, using Eq. (81), we

reduce the six director DOFs to five, three rotation parameters and two logarithmic stretch ratios, such that

$$\delta \mathbf{d}_K := \begin{Bmatrix} \delta \mathbf{d}_{1K} \\ \delta \mathbf{d}_{2K} \end{Bmatrix} = \Xi_K \begin{Bmatrix} \delta \Theta_K \\ \delta \mu_{1K} \\ \delta \mu_{2K} \end{Bmatrix}, \quad (83)$$

with

$$\Xi_K := \begin{bmatrix} -\widehat{\mathbf{d}}_{1K} & \mathbf{d}_{1K} & \mathbf{0}_{3 \times 1} \\ -\widehat{\mathbf{d}}_{2K} & \mathbf{0}_{3 \times 1} & \mathbf{d}_{2K} \end{bmatrix}_{6 \times 5}, \quad (84)$$

where  $K = 1$  for  $e = 1$  (i.e. Case 1), and  $K = n_{\text{cp}}^d$  for  $e = n_{\text{el}}$  (i.e. Case 2), see also Table A.1. Here, we also define  $\mathbf{d}_{\alpha K} := \mathbf{d}_{\alpha}^h(0)$  for  $K = 1$ , and  $\mathbf{d}_{\alpha K} := \mathbf{d}_{\alpha}^h(L)$  for  $K = n_{\text{cp}}^d$ .

**Remark 5.1.** In our computer implementation, for convenience, we introduce a fictitious DOF ( $\delta \Theta_K^*$ ) to have the same number of control coefficients at the selected boundary control points as we have at internal control points. The matrix  $\Xi_K$  is also modified to have an additional sixth column of zeros accordingly, as

$$\delta \mathbf{d}_K = \Xi_K^* \delta \mathbf{d}_K^*, \quad \text{with } \Xi_K^* := \begin{bmatrix} \Xi_K & \mathbf{0}_{6 \times 1} \end{bmatrix}_{6 \times 6}, \quad \text{and } \delta \mathbf{d}_K^* := \begin{Bmatrix} \delta \Theta_K \\ \delta \mu_{1K} \\ \delta \mu_{2K} \\ \delta \Theta_K^* \end{Bmatrix}, \quad K \in \{1, n_{\text{cp}}^d\} \quad (85)$$

Note that the fictitious DOF ( $\delta \Theta_K^*$ ) is associated with the change of the angle between two directors, which is not allowed in the rigid joint condition. The artificial DOFs are removed, together with the constrained displacement DOFs, so that they are not considered in the final reduced system of linear equations.

Thus, if the first or last element of the given NURBS patch contains a junction, we apply the transformation

$$\delta \mathbf{d}^e = \Xi^e \delta \mathbf{d}^{*e}, \quad e \in \mathcal{J}, \quad (86)$$

with

$$\Xi^e := \begin{cases} \begin{bmatrix} \Xi_1^* & \mathbf{0}_{6 \times 6(n_e^d-1)} \\ \mathbf{0}_{6(n_e^d-1) \times 6} & \mathbf{1}_{6(n_e^d-1) \times 6(n_e^d-1)} \end{bmatrix}, & \text{if } e = 1, \quad (\text{Case 1}) \\ \begin{bmatrix} \mathbf{1}_{6(n_e^d-1) \times 6(n_e^d-1)} & \mathbf{0}_{6(n_e^d-1) \times 6} \\ \mathbf{0}_{6 \times 6(n_e^d-1)} & \Xi_{n_{\text{cp}}^d}^* \end{bmatrix}, & \text{if } e = n_{\text{el}}, \quad (\text{Case 2}) \end{cases} \quad (87)$$

and we define

$$\delta \mathbf{d}^{*e} := \begin{cases} \left[ \delta \mathbf{d}_1^{*T}, \delta \mathbf{d}_2^{eT}, \dots, \delta \mathbf{d}_{n_e^d-1}^{eT}, \delta \mathbf{d}_{n_e^d}^{eT} \right]^T, & \text{if } e = 1, \quad (\text{Case 1}) \\ \left[ \delta \mathbf{d}_1^{eT}, \delta \mathbf{d}_2^{eT}, \dots, \delta \mathbf{d}_{n_e^d-1}^{eT}, \delta \mathbf{d}_{n_{\text{cp}}^d}^{*T} \right]^T, & \text{if } e = n_{\text{el}}. \quad (\text{Case 2}) \end{cases} \quad (88)$$

For convenience, we further define

$$\tilde{\Xi}^e := \begin{bmatrix} \mathbf{1}_{3n_e \times 3n_e} & \mathbf{0}_{3n_e \times 6n_e^d} \\ \mathbf{0}_{6n_e^d \times 3n_e} & \Xi^e \end{bmatrix}, \quad \text{and } \delta \tilde{\mathbf{y}}^e := \begin{Bmatrix} \delta \varphi^e \\ \delta \mathbf{d}^{*e} \end{Bmatrix}, \quad (89)$$

such that

$$\delta \mathbf{y}^e = \tilde{\mathbf{\Xi}}^e \delta \tilde{\mathbf{y}}^e. \quad (90)$$

The same transformation applies to the increment,

$$\Delta \mathbf{y}^e = \tilde{\mathbf{\Xi}}^e \Delta \tilde{\mathbf{y}}^e. \quad (91)$$

For an element that contains a junction at the end ( $e \in \mathcal{J}$ ), the internal force vector of the element is transformed, as

$$\delta \mathbf{y}^{eT} \bar{\mathbf{F}}_{\text{int}}^e = \delta \tilde{\mathbf{y}}^{eT} \tilde{\mathbf{F}}_{\text{int}}^e \quad \text{with} \quad \tilde{\mathbf{F}}_{\text{int}}^e := \tilde{\mathbf{\Xi}}^{eT} \bar{\mathbf{F}}_{\text{int}}^e, \quad (92)$$

where  $\bar{\mathbf{F}}_{\text{int}}^e$  is given in Eq. (68). In the same way, the elemental external load vector is also transformed by

$$\delta \mathbf{y}^{eT} \mathbf{F}_{\text{ext}}^e = \delta \tilde{\mathbf{y}}^{eT} \tilde{\mathbf{F}}_{\text{ext}}^e \quad \text{with} \quad \tilde{\mathbf{F}}_{\text{ext}}^e := \tilde{\mathbf{\Xi}}^{eT} \mathbf{F}_{\text{ext}}^e. \quad (93)$$

### 5.2.1. Linearization

The transformation of Eq. (86) also contributes to the geometric tangent stiffness, due to its dependence on the current directions at the junction. Applying a perturbation to the transformation matrix, Eq. (92) can be rewritten as

$$\delta \mathbf{y}_\varepsilon^{eT} \mathbf{f}_y^e = \delta \tilde{\mathbf{y}}_\varepsilon^{eT} \tilde{\mathbf{\Xi}}_\varepsilon^{eT} \mathbf{f}_y^e, \quad \varepsilon \in \mathbb{R}, \quad e \in \mathcal{J}. \quad (94)$$

Then, the directional derivative is obtained by

$$\left. \frac{d}{d\varepsilon} \left( \delta \tilde{\mathbf{y}}_\varepsilon^{eT} \tilde{\mathbf{\Xi}}_\varepsilon^{eT} \mathbf{f}_y^e \right) \right|_{\varepsilon=0} = \begin{Bmatrix} \delta \Theta_K \\ \delta \mu_{1K} \\ \delta \mu_{2K} \end{Bmatrix}^T \mathbb{K}_K \begin{Bmatrix} \Delta \Theta_K \\ \Delta \mu_{1K} \\ \Delta \mu_{2K} \end{Bmatrix} = \delta \mathbf{d}_K^{*T} \mathbb{K}_K^* \Delta \mathbf{d}_K^*, \quad (95)$$

where

$$\mathbb{K}_K = \begin{bmatrix} \mathbf{d}_{\alpha K} \otimes \tilde{\mathbf{m}}_K^\alpha - (\mathbf{d}_{\alpha K} \cdot \tilde{\mathbf{m}}_K^\alpha) \mathbf{1}_{3 \times 3} & \mathbf{m}_K^1 & \mathbf{m}_K^2 \\ \mathbf{m}_K^{1T} & \mathbf{d}_{1K} \cdot \tilde{\mathbf{m}}_K^1 & 0 \\ \mathbf{m}_K^{2T} & 0 & \mathbf{d}_{2K} \cdot \tilde{\mathbf{m}}_K^2 \end{bmatrix}_{5 \times 5}, \quad (96)$$

with a repeated index  $\alpha \in \{1, 2\}$ , and no summation implied on  $K \in \{1, n_{\text{cp}}^d\}$ .  $\tilde{\mathbf{m}}_K^\alpha$  denotes the director stress couple at the junction, which is simply obtained by the components, conjugate to  $\delta \mathbf{d}_{\alpha K}$ , in the elemental array  $\mathbf{f}_y^e$ . Note that  $\delta \mathbf{d}_{\alpha K} \equiv \delta \mathbf{d}_{\alpha I}^e$ , based on the correspondence between indices  $e$ ,  $I$ , and  $K$  in each of the cases 1 and 2, see Table A.1. We also define the moment at the junction,  $\mathbf{m}_K^\alpha := \mathbf{d}_{\alpha K} \times \tilde{\mathbf{m}}_K^\alpha$  (no sum on  $\alpha \in \{1, 2\}$ ). In the second equality of Eq. (95), we also introduce the fictitious fifth row and columns of zeros,

$$\mathbb{K}_K^* = \begin{bmatrix} \mathbb{K}_K & \mathbf{0}_{5 \times 1} \\ \mathbf{0}_{1 \times 5} & 0 \end{bmatrix}_{6 \times 6}. \quad (97)$$

Then, the geometrical element tangent stiffness matrix due to the joint condition for the  $e$ th element ( $e \in \mathcal{J}$ ) is obtained by

$$\tilde{\mathbb{K}}^e = \begin{bmatrix} \mathbf{0}_{3n_e \times 3n_e} & \mathbf{0}_{3n_e \times 6n_e^d} \\ \mathbf{0}_{6n_e^d \times 3n_e} & \mathbb{K}^e \end{bmatrix}, \quad (98)$$

with

$$\mathbb{K}^e := \begin{cases} \begin{bmatrix} \mathbb{K}_1^* & \mathbf{0}_{6 \times 6(n_e^d-1)} \\ \mathbf{0}_{6(n_e^d-1) \times 6} & \mathbf{0}_{6(n_e^d-1) \times 6(n_e^d-1)} \end{bmatrix}, & \text{if } e = 1, \quad (\text{Case 1}) \\ \begin{bmatrix} \mathbf{0}_{6(n_e^d-1) \times 6(n_e^d-1)} & \mathbf{0}_{6(n_e^d-1) \times 6} \\ \mathbf{0}_{6 \times 6(n_e^d-1)} & \mathbb{K}_{n_{ep}^d}^* \end{bmatrix}, & \text{if } e = n_{e1}. \quad (\text{Case 2}) \end{cases} \quad (99)$$

Applying the transformation of Eqs. (90) and (91), and adding the additional geometric tangent stiffness of Eq. (98), we obtain the tangent stiffness matrix of the element containing the joint, as

$$\bar{\mathbb{K}}_{\text{int}}^e = \tilde{\mathbf{\Xi}}^{eT} \bar{\mathbb{K}}_{\text{int}}^e \tilde{\mathbf{\Xi}}^e + \tilde{\mathbb{K}}^e, \quad e \in \mathcal{J}, \quad (100)$$

where  $\bar{\mathbb{K}}_{\text{int}}^e$  is given in Eq. (65). Then, considering the joint condition, Eq. (64) can be rewritten as

$$\delta \tilde{\mathbf{y}}^T \bar{\mathbb{K}} \Delta \tilde{\mathbf{y}} = \delta \tilde{\mathbf{y}}^T \bar{\mathbb{F}}, \quad (101)$$

where

$$\bar{\mathbb{K}} := \mathbf{A}_{e \notin \mathcal{J}} \bar{\mathbb{K}}_{\text{int}}^e + \mathbf{A}_{e \in \mathcal{J}} \bar{\mathbb{K}}_{\text{int}}^e, \quad (102)$$

and

$$\bar{\mathbb{F}} := \mathbf{A}_{e \notin \mathcal{J}} (\mathbf{F}_{\text{ext}}^e - \bar{\mathbf{F}}_{\text{int}}^e) + \mathbf{A}_{e \in \mathcal{J}} (\tilde{\mathbf{F}}_{\text{ext}}^e - \tilde{\mathbf{F}}_{\text{int}}^e) + \mathbf{A} [\bar{\mathbf{R}}_0]_{s \in \Gamma_N}. \quad (103)$$

After removing the rows and columns corresponding to the DOFs of homogeneous boundary conditions and fictitious DOFs (see Remark 5.1) in the joint conditions, we obtain the system of linear equations

$$\bar{\mathbb{K}}_r \Delta \tilde{\mathbf{y}}_r = \bar{\mathbb{F}}_r, \quad (104)$$

where the subscript  $(\bullet)_r$  in Eq. (104) denotes the *reduced* vector or matrix.

**Remark 5.2.** *Symmetry of tangent stiffness matrix at equilibrium.* It appears that this additional geometric tangent stiffness matrix due to the joint condition is generally non-symmetric due to the term  $\mathbf{d}_{\alpha K} \otimes \tilde{\mathbf{m}}_K^\alpha$ . It has been discussed in Simo and Vu-Quoc (1986) that the presence of a rotation group, which is a nonlinear manifold, in configuration space leads to the non-symmetry; however, they also proved that the skew-symmetric part of the geometric tangent stiffness operator vanishes at the equilibrium configuration. In a similar manner, we further examine the skew-symmetric part of the tangent stiffness matrix, i.e.,  $\tilde{\mathbb{K}}_K^A := \frac{1}{2} (\tilde{\mathbb{K}}_K - \tilde{\mathbb{K}}_K^T)$ , which gives

$$\delta \Theta_K \cdot \tilde{\mathbb{K}}_K^A \Delta \Theta_K = \delta \Theta_K \cdot \frac{1}{2} (\mathbf{d}_{\alpha K} \otimes \tilde{\mathbf{m}}_K^\alpha - \tilde{\mathbf{m}}_K^\alpha \otimes \mathbf{d}_{\alpha K}) \Delta \Theta_K = \frac{1}{2} \delta \Theta_K \times \mathbf{m}_K^\alpha \cdot \Delta \Theta_K. \quad (105)$$

Then, for multiple beams (NURBS patches) connected to a joint with rotational continuity condition, we rewrite Eq. (105) as

$$\sum_{i=1}^N (\delta \Theta_K \cdot \tilde{\mathbb{K}}_K^A \Delta \Theta_K)_i = \delta \Theta \times \sum_{i=1}^N (\mathbf{m}_K^\alpha)_i \cdot \Delta \Theta, \quad (106)$$

where the subscript  $(\bullet)_i$  denotes that the quantity belongs to  $i$ -th constituent beam (patch), and  $N$  denotes the total number of connected beams. We also use  $(\delta \Theta_K)_1 = \dots = (\delta \Theta_K)_N =: \delta \Theta$  and  $(\Delta \Theta_K)_1 = \dots = (\Delta \Theta_K)_N =: \Delta \Theta$  due to the rotational continuity. By the moment equilibrium at the joint,

$$\sum_{i=1}^N (\mathbf{m}_\alpha^K)_i = \mathbf{0}. \quad (107)$$

Therefore, the skew-symmetric part of the tangent stiffness matrix vanishes at equilibrium. That is, in the *equilibrium configuration*, the symmetry of the global tangent stiffness matrix solely depends on whether the external loading is conservative. In *non-equilibrium configurations*, the additional geometrical tangent stiffness due to the rotational continuity conditions leads to an unsymmetric tangent stiffness matrix.

### 5.2.2. Configuration update procedure

For an end control points under the joint condition, the update process in Eq. (70b) should be replaced by a *multiplicative* one for an *exact* update. Using Eq. (45), the end directors are decomposed into

$${}^{n+1}\mathbf{d}_{\alpha K}^{(i)} = {}^{n+1}\lambda_{\alpha K}^{(i)} {}^{n+1}\mathbf{t}_{\alpha K}^{(i)}, \quad (108)$$

where the finite rotation of the unit director, due to the (finite) incremental rotation  $\Delta\Theta^{(i)}$ , can be expressed by (Argyris, 1982)

$${}^{n+1}\mathbf{t}_{\alpha K}^{(i)} = \exp\left[\widehat{\Delta\Theta}^{(i)}\right] {}^{n+1}\mathbf{t}_{\alpha K}^{(i-1)}, \quad {}^{n+1}\mathbf{t}_{\alpha K}^{(0)} \equiv {}^n\mathbf{t}_{\alpha K}, \quad (109)$$

with

$$\exp\left[\widehat{\Delta\Theta}\right] = \mathbf{1} + \frac{\sin\Theta}{\Theta}\widehat{\Delta\Theta} + \frac{1 - \cos\Theta}{\Theta^2}\widehat{\Delta\Theta}^2, \quad \text{with } \Theta := \|\Delta\Theta\| \neq 0, \quad (110)$$

which becomes the identity tensor if  $\Theta = 0$ . The stretch ratio is also updated by the (finite) increment of the logarithmic stretch  $\Delta\mu_{\alpha K}^{(i)}$ , as

$${}^{n+1}\lambda_{\alpha K}^{(i)} = \exp\left[{}^{n+1}\mu_{\alpha K}^{(i)}\right], \quad (111)$$

with

$${}^{n+1}\mu_{\alpha K}^{(i)} = {}^{n+1}\mu_{\alpha K}^{(i-1)} + \Delta\mu_{\alpha K}^{(i)}, \quad {}^{n+1}\mu_{\alpha K}^{(0)} \equiv {}^n\mu_{\alpha K}. \quad (112)$$

**Remark 5.3.** It should be noted that the presented configuration update procedure does not require any secondary storage for the cross-sectional orientation and stretch at the previous iteration step, i.e.  ${}^{n+1}\mathbf{t}_{\alpha K}^{(i-1)}$ , and  ${}^{n+1}\mu_{\alpha K}^{(i-1)}$ , respectively. This is due to the fact that they can be simply calculated by using the primary control coefficients of director displacement  $\bar{\mathbf{d}}_K$  ( $K \in \{1, n_{cp}^d\}$ ) in Eq. (45), that is, the displacement of directors at the joint.

## 6. Numerical examples

In the subsequent numerical examples, we compare the following two approaches in the proposed mixed formulation within the framework of IGA:

- a **global** approach (“**glo**”) using NURBS basis functions of degree  $p_p = p - 1$  for the physical stress resultant and strain fields having  $C^{p_p-1}$  inter-element continuity, which is combined with a patch-wise static condensation,
- a **local** approach (“**loc**”) allowing inter-element discontinuity of the physical stress resultant and strain fields, which is combined with an element-wise static condensation.

In FEA, we use only the local approach. In both approaches, we use full Gauss integration along the axis (“FI”). For the integration over the cross-section, we also use Gauss integration considering  $3 \times 3$  quadrature points.

### 6.1. Cantilever beam under bending moment

We consider an initially straight beam of length  $L = 10$  m with a rectangular cross-section of width  $w = 1$  m and thickness  $h$ . A St. Venant-Kirchhoff type material is considered, with Young's modulus  $E = 1.2 \times 10^7$  Pa, and Poisson's ratio  $\nu = 0$ . The beam's left-end is constrained, and the other end is subject to a moment load  $M = 2\pi EI/L$ , where  $I = wh^3/12$  denotes the second area moment of inertia of the cross-section, see Fig. 4. The moment load is applied by a distributed follower load on the cross-section at the right-end, whose expressions of the external virtual work and its increment can be found in Choi et al. (2021). At the left-end, the cross-section's translation and rotation are constrained, but the transverse normal (through-the-thickness) stretching is allowed, so that

$$\varphi = \varphi_0, \Delta d_{11} = \Delta d_{12} = 0, \text{ and } \Delta d_{13} \text{ is free,} \quad (113)$$

where  $\Delta d_{\alpha i} := \Delta \mathbf{d}_\alpha \cdot \mathbf{e}_i$ . For the given problem, we have an analytical solution for the thin beam limit (pure bending condition), such that the moment  $M$  deforms the beam's axis into a circle with radius  $R = EI/M$ .

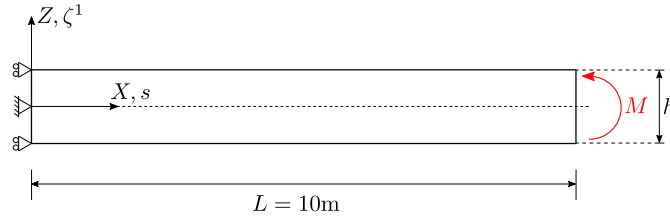


Figure 4: Cantilever beam under bending moment. Geometry and boundary conditions. Note that the thickness stretch ( $\Delta d_{13}$ ) is free at  $s = 0$ .

#### 6.1.1. Alleviation of locking for $p = 2$ in IGA by reducing $p_d$

Figs. 5a and 5b show the distribution of the transverse shear strain along the beam's axis resulting from FEA and IGA, respectively. In both cases, we use uniformly reduced integration (URI). The FEA result shows that the positions of the Gauss quadrature points in every element coincide with the zeros of the transverse shear strain, which is discontinuous across the elements. Thus, transverse shear locking can be alleviated by URI in FEA. However, in the IGA results, it is seen that the continuous strain distribution vanishes in other locations than the Gauss quadrature points. This means that an element-wise reduced integration is not an effective tool for IGA to alleviate transverse shear locking. Transverse shear locking can be explained by the field-inconsistency paradigm (Prathap, 2013). To circumvent this inconsistency, we may consider to use one degree lower basis functions for the director field. In Fig. 6, we investigate the effectiveness of using  $p_d = p - 1$  to alleviate the transverse shear locking. Note that it is combined with full Gauss integration along the axis ("FI").

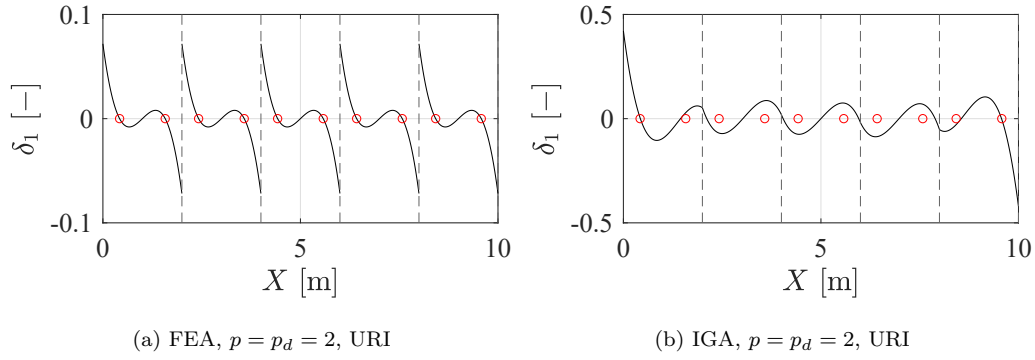


Figure 5: Cantilever beam under bending moment: Comparison of the transverse shear strain distribution along the beam's axis according to FEA and IGA. The slenderness ratio is  $L/h = 10^2$ . In both cases, we use quadratic basis functions, and five elements. In every element, we use two Gauss quadrature points ( $n_G = 2$ ), i.e. uniformly reduced integration (URI). The hollow red circles represent the positions of the Gauss quadrature points, and the dashed vertical lines represent the element boundaries. All results are obtained from the displacement-based formulation.

We first recall the expressions of the bending, membrane (axial), and transverse normal (through-the-thickness) strain energies in [Choi et al. \(2021\)](#),

$$\Pi_\rho := \int_0^L \tilde{m}^1 \rho_1 ds \sim h^3, \quad (114)$$

$$\Pi_\varepsilon := \int_0^L \tilde{n} \varepsilon ds \sim h^5, \quad (115)$$

and

$$\Pi_\chi := \int_0^L \tilde{t}^{11} \chi_{11} ds \sim h^5, \quad (116)$$

respectively. Therefore, the ratios  $\Pi_\varepsilon/\Pi_\rho$  and  $\Pi_\chi/\Pi_\rho$  should decrease quadratically with decreasing the initial cross-sectional thickness  $h$ . Further, the transverse shear strain energy should also be proportional to  $h^5$ , i.e.

$$\Pi_\delta := \int_0^L \tilde{q}^1 \delta_1 ds \sim h^5. \quad (117)$$

In the calculation of the strain energies in Eqs. (115)-(117), we use

- compatible strains in Eq. (7), with the approximated displacements, for the **displacement-based** formulation,
- approximated physical stress resultants in Eq. (51), and physical strains in Eq. (52) for the **mixed** formulation.

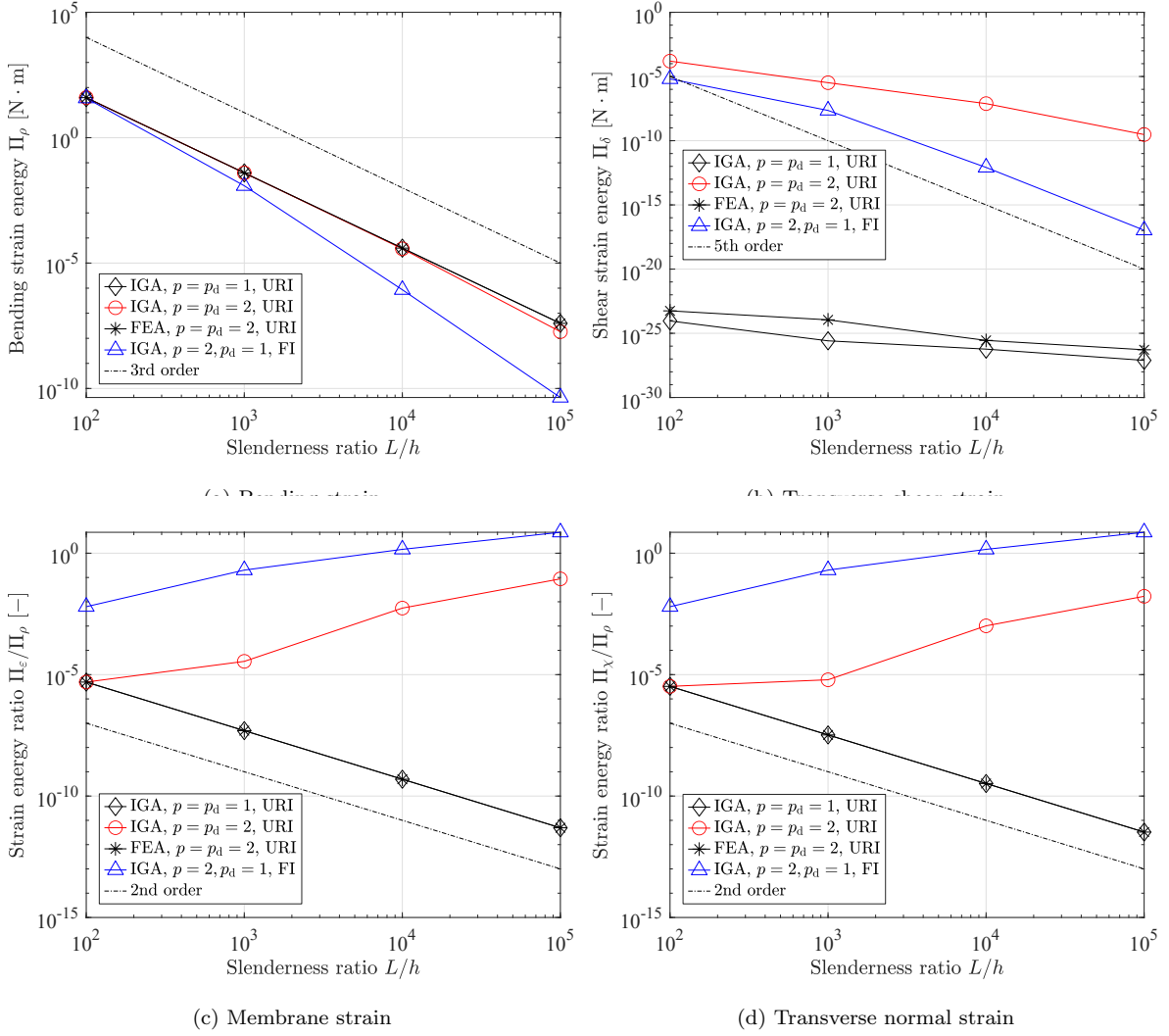


Figure 6: Cantilever beam under bending moment: Comparison of the strain energies resulting from different selection of  $p_d$ , including the cases of using (i) the same degree of basis  $p = p_d = 1, 2$  with the uniformly reduced integration (URI), and (ii) different degree of basis  $p = 2$  and  $p_d = 1$  with three Gauss quadrature points per element ( $n_G = 3$ ), i.e. full integration (FI). Note that IGA using  $p = 1$  gives the same result as FEA using  $p = 1$ . All results are from the displacement-based formulation.

Fig. 6a shows that the FEA results with  $p = 2$  and URI (black curve) exhibits a cubic rate of decrease of the bending strain energy, as expected by Eq. (114). However, the result from IGA with  $p = 2$  and URI (red curve) shows, as expected, slight deviation from the analytical rate of decrease due to locking. In IGA, only in the case of  $p = 1$ , it shows the correct decrease rate, since it has no inter-element continuity in the strain fields, as in FEA. It is also seen that IGA with  $p = 2$  and  $p_d = 1$  (blue curve) suffers from severe locking. We compare the decrease rate of the strain energy with the analytical solution in Eqs. (115)-(116). In Fig. 6b, it is seen that the approach of using  $p_d = p - 1$  (blue curve) yields much smaller transverse shear strain energy than that from IGA ( $p = 2$ ) with URI (red curve). In Figs. 6c and 6d, it is seen that the IGA results show spurious increase in both of the membrane, and transverse normal strains. In contrast, the results having no inter-element continuity in the strain fields (black curves) show the quadratic rate of decrease in both cases. This adverse effect of higher order continuity



in IGA can be also observed in results from the mixed formulation. In Fig. 7, we investigate the decrease rate of the strain energy, obtained by using the mixed formulation, for different cases of  $p_d$  and the inter-element continuity of the strains.

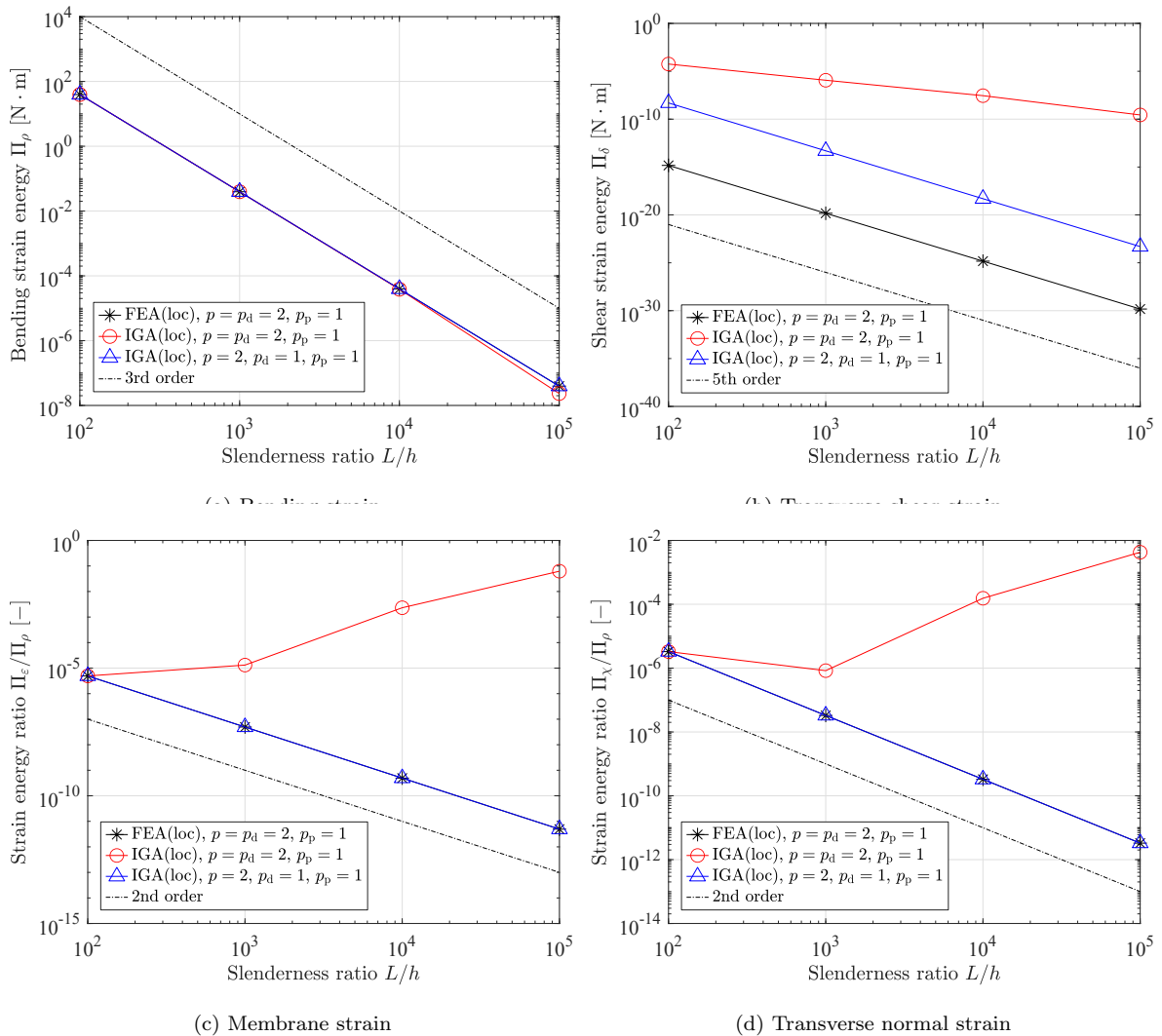
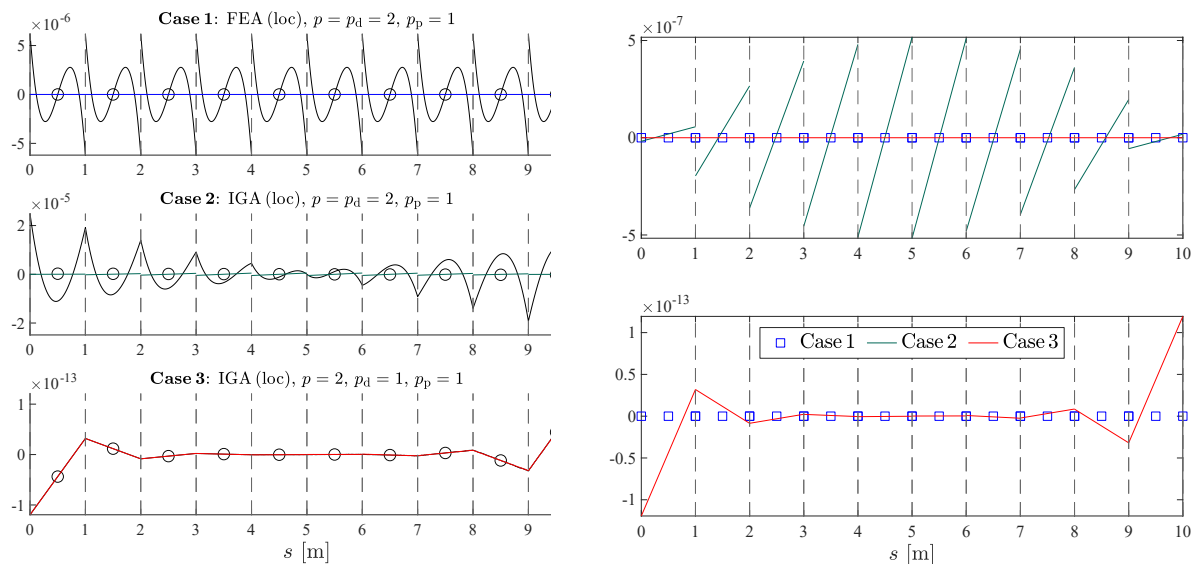


Figure 7: Cantilever beam under bending moment: Comparison of the strain energies resulting from different selection of  $p_d$ , including the cases of using (i) the same degrees of bases  $p = p_d = 2$ , and (ii) different degrees of bases  $p = 2$  and  $p_d = 1$ , and  $p_p = 1$ . All results are from the mixed formulation with  $p_p = 1$ , combined with the local approach (“loc”), and full integration along the axis ( $n_G = 3$ ).

In Fig. 7, it is seen that the IGA using the mixed formulation, combined with a local (element-wise) static condensation (red curve), suffers from severe locking, see spurious strain energy in Figs. 7b-7d, and the spuriously higher decrease rate of the bending strain energy in Fig. 7a. This is due to the fact that it does not consider the locking effect arising from the continuity condition of the strain fields. Surprisingly, if we reduce  $p_d$  to 1, the transverse shear strain vanishes at fifth order rate, as in the FEA result, and all the other spurious strain energies also vanish.

In order to further investigate the alleviation of locking, we compare the distribution of the axial ( $\varepsilon$ ), transverse shear ( $\delta_1$ ), transverse normal ( $\chi_{11}$ ), and couple shear ( $\gamma_{11}$ ) strains along the axis, resulting from three different finite element approximations of the mixed formulation using  $p = 2$ . Fig. 8 compares

the distribution of the transverse shear strain. In every case shown in Fig. 8, the physical strain agrees very well with the element-wise average of the geometrical strain (black hollow circles), which means the compatibility condition is weakly satisfied well. For the polynomial basis functions of  $p = p_d = 2$ , the transverse shear strain  $\delta_1$  of Eq. (7c) is a cubic polynomial. In Fig. 8a, the FEA result (Case 1) clearly shows the cubic (black) curve within each element; however, in the IGA result (case 2), the geometric strain field in each element (black curve) is very close to a quadratic function. This is attributed to the additional constraints in IGA for the inter-element  $C^0$ -continuity of  $\delta_1$ , and it eventually leads to oscillatory distribution of the physical strains to satisfy the compatibility condition. In the FEA result (Case 1), the geometric strain does not vanish, but the corresponding physical strain, using the degree of basis  $p_p = 1$ , vanishes properly, see also the physical strain distribution (green square markers) in Fig. 8b. In contrast, the IGA results with the same degrees of bases  $p = p_d = 2$ , and  $p_p = 1$  (case 2) shows a significant amount of the transverse shear strain, which leads to a severe (artificial) increase of the bending stiffness. By decreasing the degree  $p_d$  in case 3, the transverse shear locking is effectively alleviated. It is noticeable that the geometrical strain also vanishes, in contrast to the FEA result using  $p_d = p = 2$  (Case 1).



(a) Comparison of the geometrical and physical strains

(b) Physical strains (bottom: cases 1 and 3 only)

Figure 8: Cantilever beam under bending moment: Distribution of the **transverse shear** strain  $\delta_1$  along the axis. (a) Comparison of the geometrical (black curves) and physical strains (colored curves) along the axis, obtained by three different formulations (Cases 1-3). In the result of Case 3, the black and red curves are overlapping. (b) Those physical strains in (a) are re-plotted in the common ordinate. In all results, we use ten elements ( $n_{el} = 10$ ), and the selected slenderness ratio is  $L/h = 10^5$ . The dashed lines represent the element boundaries, and the hollow circles in (a) represent element-wise average of the geometric strain.

Fig. 9 compares the distribution of the transverse normal strain (through-the-thickness stretch), and the couple shear strain along the axis. For degree  $p_d = p = 2$  polynomial bases of director displacements, the transverse normal strain  $\chi_{11}$  in Eq. (7e) is a quartic polynomial. Similar to the previous case of transverse shear strain distribution, it is observed in Fig. 9a that the geometric strain field in the result of only case 2

is closer to a cubic function within each element, but the FEA result shows a quartic distribution of the geometric strain in each element. In case 3, we use  $p_d = p - 1 = 2$ , so that  $\chi_{11}$  is a quadratic polynomial, see the parabolic (black) curve in the result of case 3 in Fig. 9a. The geometrical couple shear strain  $\gamma_{11}$  is one degree lower than  $\chi_{11}$ , due to  $\gamma_{11} = \chi_{11,s}$ , see the geometric strains (black curves) in Fig. 9b. Here we observe an inconsistency between the strain fields  $\gamma_{11}$  and  $\chi_{11,s}$ , i.e.  $\gamma_{11} \neq \chi_{11,s}^p$ , in both cases 1 and 3. However, this couple shear strain is a higher order strain than the transverse shear strain, in terms of the transverse coordinate  $\zeta^1$  in the Green-Lagrange strain component  $E_{31}$ , see Eq. (6). Thus, it may not significantly affect the overall response in thin beams. Further alleviation of this inconsistency remains future work.

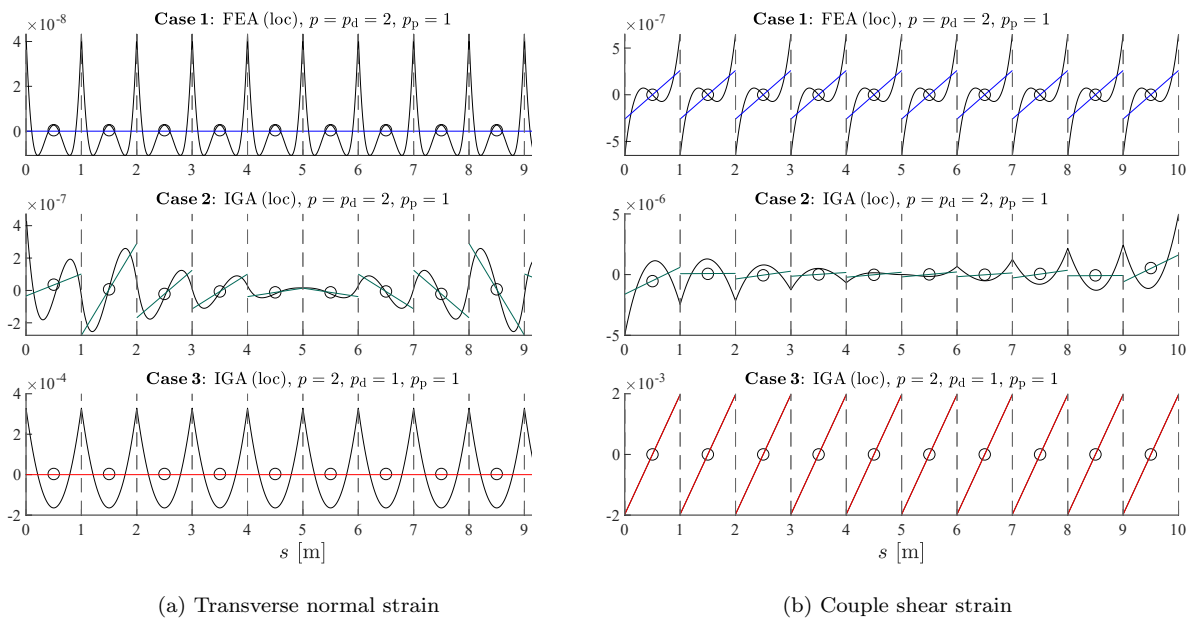
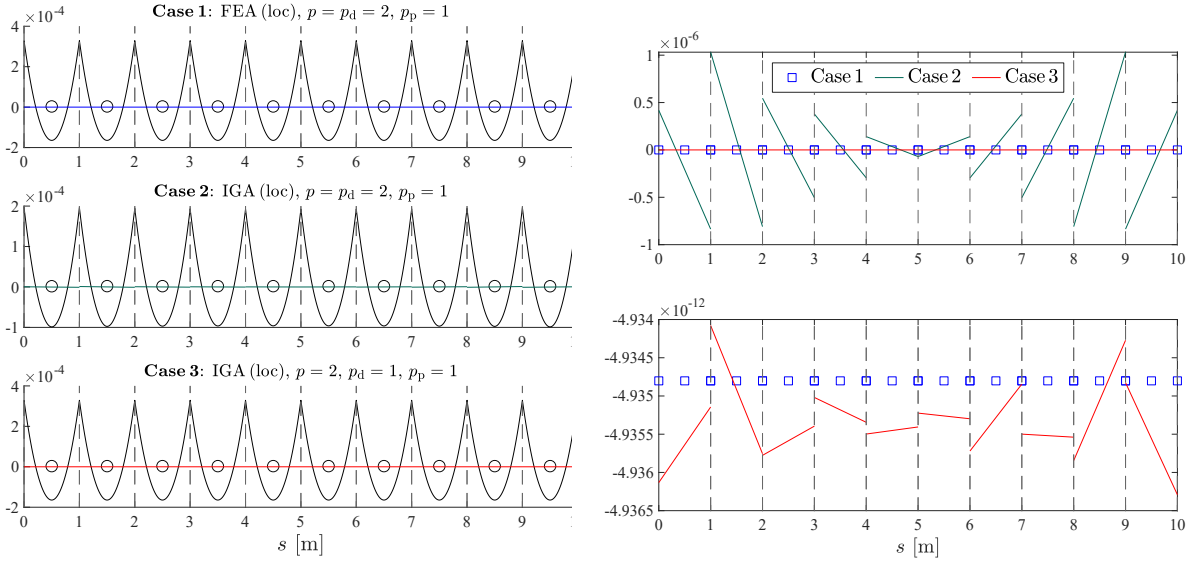


Figure 9: Cantilever beam under bending moment: Distribution of the **transverse normal** ( $\chi^{11}$ ), and **couple shear** ( $\gamma^{11}$ ) strains along the axis. The geometrical (black curves) and physical (colored curves) strains in the three cases of the mixed formulation are compared. The hollow circles represent the element-wise average of the geometrical strain. In all results,  $n_{el} = 10$ , and  $L/h = 10^5$ . The dashed lines represent the element boundaries.

Fig. 10 compares the distribution of the axial (membrane) strain along the axis. For the degree  $p$  polynomial bases of the axial displacement, the axial strain is a quadratic polynomial, see the parabolic (black) curves for the geometric strains in Fig. 10a. In Fig. 10a, the physical strain in case 2 shows slight discontinuities across the elements, which can be more clearly seen in Fig. 10b. Thus, in full Gauss integration along the axis, the spurious membrane strain is evaluated, which also contributes to the artificial increase of the bending stiffness. It is remarkable that, when we reduce the degree  $p_d$ , the spurious physical axial strain vanishes. Although the director is not explicitly associated with the axial strain, the alleviation of the other spurious strain may affect the axial deformation as well in geometrically nonlinear problems.



(a) Comparison of the geometrical and physical strains

(b) Comparison of the physical strains only

Figure 10: Cantilever beam under bending moment: Distribution of the **axial** strain  $\varepsilon$  along the axis. (a) Comparison of the distribution of the geometrical (black curves) and physical (colored curves) axial strains along the axis in the three cases. The hollow circles in (a) represent element-wise average of the geometric strain. (b) Those physical strains in (a) are re-plotted in the common ordinate. In all results,  $n_{el} = 10$ , and  $L/h = 10^5$ . The dashed lines represent the element boundaries.

However, in the following, it will be shown that the system is again significantly over-stiffened, as we increase the order of basis functions,  $p$ , and  $p_d = p - 1$ . To alleviate this, for  $p > 2$ , we additionally adjust the degree  $p_p$  of the basis functions for the additional fields, physical stress resultants and strains.

### 6.1.2. Alleviation of locking for $p = 3$ and $p_d = 2$ in IGA by reducing $p_p$

Fig. 11 compares the convergence rate of strain energies resulting from using  $p_p = p - 1 = 2$  and  $p_p = 1$ . In both cases, we use the mixed formulation with IGA,  $p = 3$  and  $p_d = 2$ , combined with the local approach. In the results from using  $p_p = p - 1 = 2$ , deteriorated convergence is clearly observed in Figs. 11b-11d (black curves). Interestingly, the decrease rate of the transverse shear strain energy approaches the analytical one (fifth order), as we increase the slenderness ratio. This shows the effect of using the reduced  $p_d = p - 1$ . It is remarkable that, when we choose the degree  $p_p = 1$ , the correct decrease rate is achieved in all cases (red curves).

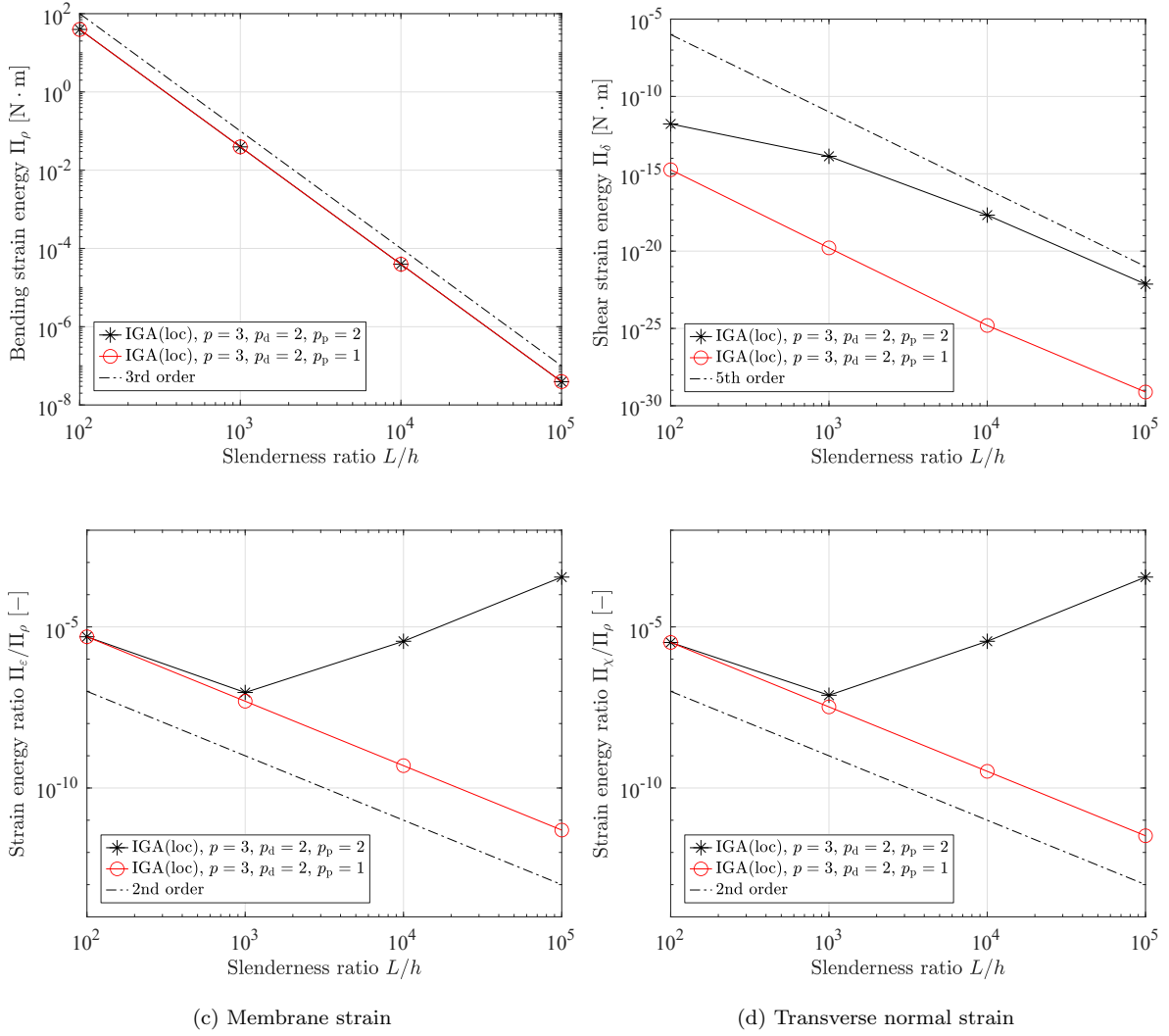


Figure 11: Cantilever beam under bending moment: Comparison of the strain energy from the different  $p_p$ , (i)  $p_p = 1$ , and (ii)  $p_p = 2$ . All results are from the mixed formulation with  $p = 3$  and  $p_d = 2$ , combined with local (element-wise) static condensation (“loc”), and full integration ( $n_G = 4$ ).

In the following two sections, we verify the advantages of IGA in terms of the computational accuracy and efficiency over the conventional FEA, due to the higher order continuity in the NURBS basis functions.

### 6.1.3. Verification of the superior convergence behavior of IGA in $h$ -refinement

We verify the convergence rate of the presented mixed isogeometric beam formulation, with the reduced degrees of bases,  $p_d$  and  $p_p$ . We compare the IGA results with the FEA results using the Lagrange polynomial bases of degree  $p$ . In FEA, we use  $p = p_d$ , and the following two different formulations to alleviate locking,

- the displacement-based formulation with a uniform reduced integration along the axis (URI) with  $n_G = p$ ,
- the mixed formulation with the degree of bases  $p_p = p - 1$  for the additional fields of the physical stress resultants and strains.

For all the IGA and FEA results based on the mixed formulation, we use  $n_G = p + 1$  Gauss integration points for the exact (full) integration. For the given problem, we have an analytical solution in the thin beam limit (pure bending condition), in which the  $X$ -displacement of the center axis is expressed by

$$u_{\text{ref}} = R \sin \frac{X}{R} - L. \quad (118)$$

For the following verification of the numerical solutions, we utilize the relative  $L^2$  norm of the difference in the  $X$ -displacement ( $u$ ) along the center axis

$$\|e_u\|_{L^2} := \sqrt{\frac{\int_0^L (u - u_{\text{ref}})^2 ds}{\int_0^L u_{\text{ref}}^2 ds}}. \quad (119)$$

Fig. 12 compares the convergence of this quantity between the results of FEA and IGA. Figs. 12a and 12b plot the same results with different abscissae: the number of elements, and the number of DOFs, respectively. In Fig. 12a, it is seen that the FEA results using the displacement-based formulation with URI (black curves with hollow markers) shows the same rate of convergence with as FEA results using mixed formulation (black curves with filled markers) for all degrees of bases,  $p = 1, 2, 3$ , but the mixed formulation gives more accurate results due to more accurate numerical integration. Further, in cases of very high beam slenderness ratio, the URI requires much more iterations in the Newton-Raphson process, compared with the mixed formulation, which will be shown in Section 6.1.5. In the IGA results (red and magenta curves), even though we use  $p_d = p - 1$ , one degree lower than that of FEA ( $p_d = p$ ), the convergence rate still agrees very well with the analytical (asymptotic) rate (order  $p + 1$ ). Fig. 12b clearly shows that IGA gives superior per DOF accuracy, compared with conventional FEA. It should be noted that the number of DOFs in Fig. 12b only contains the displacement DOFs. In the case of  $p = 3$ , IGA uses much fewer internal DOFs than FEA, due to the lower  $p_p$  for the former, and the difference is proportional to the number of elements.

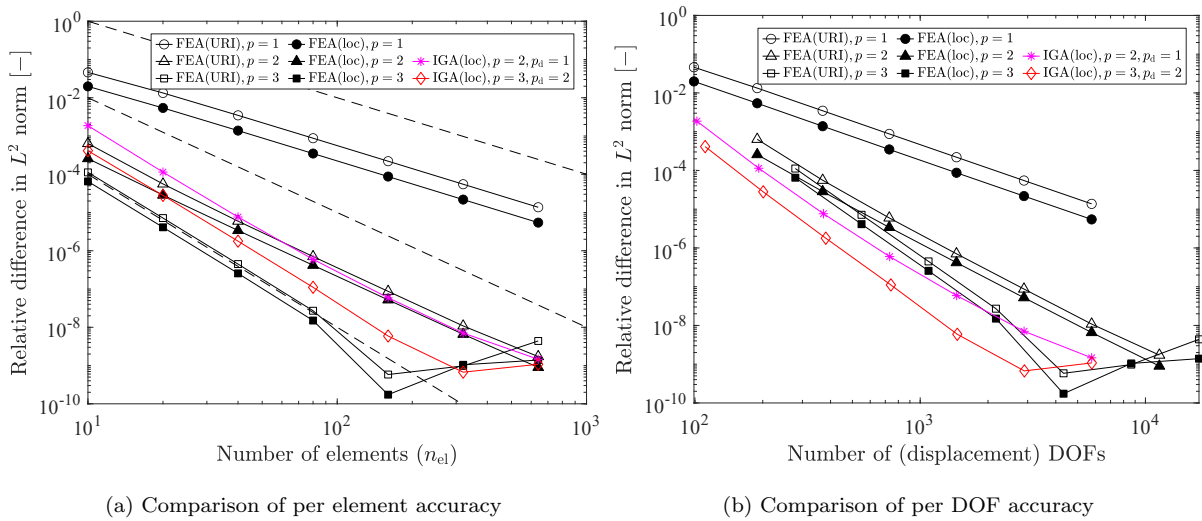


Figure 12: Cantilever beam under bending moment: Comparison of the relative difference  $\|e_u\|_{L^2}$  in FEA and IGA results. The dashed lines in (a) represent the analytical solution of asymptotic convergence rate, order  $p + 1 = 2, 3, 4$ . The selected slenderness ratio is  $L/h = 10^5$ . In all IGA results, we use  $p_p = 1$ , but for FEA results, we use  $p_p = p - 1$ .

#### 6.1.4. Further comparison: $k$ -refinement in IGA vs. $p$ -refinement in FEA

We verify the superior convergence behavior of IGA in  $k$ -refinement (smooth degree elevation) over classical  $p$ -refinement (degree elevation) in FEA. The advantage of  $k$ -refinement is that it enables to maintain the maximum  $C^{p-1}$ -continuity in the displacement field with bases of degree  $p$ , in contrast to the  $C^0$ -continuity from  $p$ -refinement (Hughes et al., 2005). We also observe an instability of IGA with uniform reduction of the degree  $p_p$  for very high degree  $p \geq 8$ , but this turns out to be alleviated by increasing the number of elements. In Fig. 13, we compare the following three different approaches of the IGA-based mixed formulation with the FEA-based one,

- the global approach (“glo”),
- the local approach (“loc”) with  $p_d = p$ , and  $p_p = p - 1$ ,
- the local approach (“loc-r”) with the reduced degrees  $p_d = p - 1$ , and  $p_p = 1$ .

In Fig. 14, we further compare the sparsity patterns and the number of nonzero components ( $\#nzc$ ) of the tangent stiffness matrix in the four chosen cases. We choose the cases giving the relative difference around  $10^{-7}$  in Fig. 13 (dashed line): (i) FEA with  $p = p_d = 5$  and  $p_p = 4$ , (ii) IGA (glo) with  $p = p_d = 6$  and  $p_p = 5$ , and (iii) IGA (loc) with  $p = 7$ ,  $p_d = 6$  and  $p_p = 1$ , and (iv) IGA (loc) with  $p = 6$ ,  $p_d = 5$  and  $p_p = 1$ . Fig. 13 shows that the IGA-based mixed formulation (loc) without reducing the degrees  $p_d$  and  $p_p$  (black curve with triangle markers) exhibits severe locking, which arises due to the discontinuous fields of physical stress resultants and strains, which cannot resolve the parasitic strains from the higher order continuity conditions in the displacement field. Even though the global approach of IGA-based mixed formulation (blue curve with square markers) gives remarkable improvement of the accuracy, it is computationally prohibitive, due to (i) the inversion of the full (global) Gram matrix in the condensation process, and (ii) the resulting dense tangent stiffness matrix, see Fig. 14b. In contrast, the presented IGA-based mixed formulation (loc-r) with reduced degrees  $p_d = p - 1$  and  $p_p = 1$  (red curve with star markers) gives comparable accuracy as the global IGA approach, at much lower computational cost, due to (i) element-wise (local) condensation, (ii) sparsity of the resulting tangent stiffness matrix, see Figs. 14c and 14d, and (iii) much fewer number of displacement and internal DOFs due to the reduced degrees  $p_d$  and  $p_p$ . However, in the results of IGA (loc-r) with  $n_{el} = 10$ , we observe that the performance (i.e. convergence rate with increasing degree  $p$ ) is much better in the range of degree  $5 \leq p \leq 7$ , compared with other degrees. In cases of very high degrees,  $p = 9, 10$ , the solution process even diverges. This result indicates that in the range  $2 \leq p \leq 4$ , the system<sup>3</sup> is over-constrained, whereas, in the range of  $8 \leq p \leq 10$ , the system is under-constrained. This can be alleviated by increasing the number of elements ( $n_{el}$ ), see the results from  $n_{el} = 20$  (cyan curve), which exhibit remarkable per DOF accuracy.

<sup>3</sup>the system of linear equations in the iterative solution process

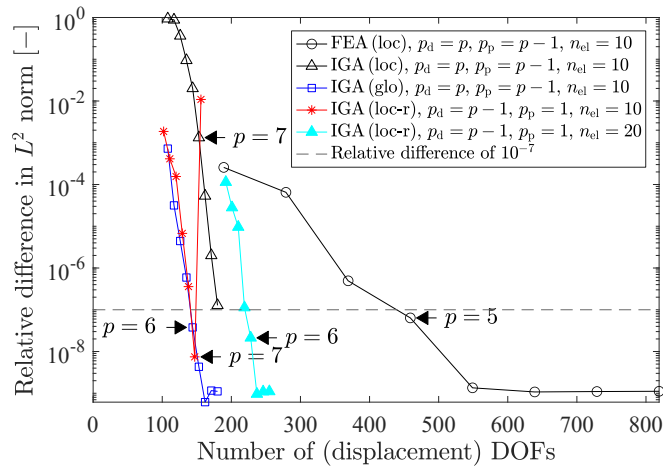


Figure 13: Cantilever beam under bending moment: Comparison of the results from the  $k$ -refinement in IGA with the  $p$ -refinement in FEA for the relative difference of the  $X$ -displacement *per displacement DOF*. In each graph, the markers represent the results of using  $p = 2, 3, \dots, 10$ . In all cases we use the mixed formulation. IGA (loc-r) diverges from  $p = 9$  and  $p = 10$  onward for  $n_{el} = 10$  and  $n_{el} = 20$ , respectively, so those data are not shown. The slenderness ratio is  $L/h = 10^5$ .



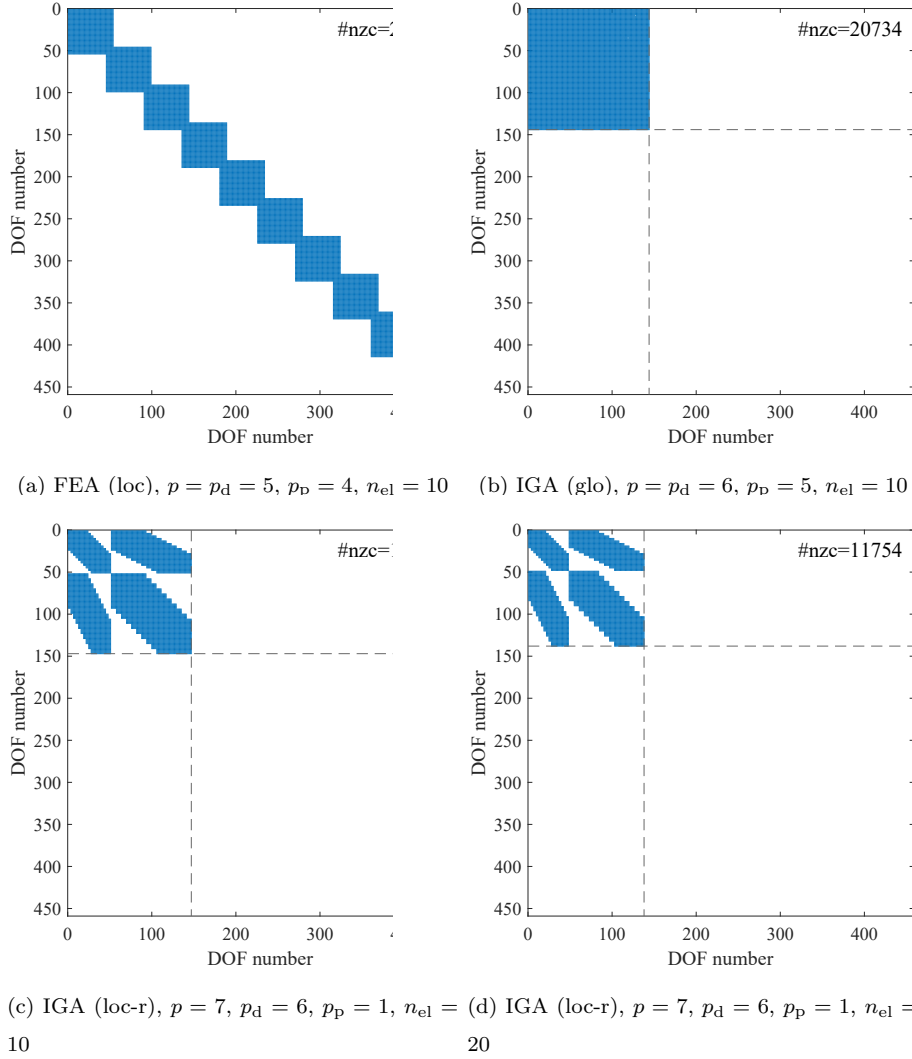


Figure 14: Cantilever beam under bending moment: comparison of the sparsity pattern in the tangent stiffness matrix at the first iteration of the last (10th) load step. Here #nzc denotes the number of nonzero components. Figures (b) and (c) are shown in the same scale as (a) for comparison.

In order to further investigate the stability of the proposed mixed formulation with  $p_d = p - 1$  and  $p_p = 1$ , we calculate the natural frequencies of the straight beam by solving an eigenvalue problem at the initial configuration. We solve a generalized eigenvalue problem without any displacement boundary conditions

$$\bar{\mathbf{K}} \Delta \mathbf{y} = \omega^2 \mathbf{M} \Delta \mathbf{y}, \quad (120)$$

where  $\omega$  denotes the angular (natural) frequency, and  $\bar{\mathbf{K}}$  denotes the global tangent stiffness matrix in Eq. (65), and  $\mathbf{M}$  denotes the global mass matrix (see Appendix B for its detailed expression). As we consider no displacement boundary conditions, i.e. free-free ends of the beam, the eigenvalue problem of Eq. (120) correctly reproduces the first six zero eigenvalues, associated with the rigid body motions. Here, all the results are calculated by the proposed mixed isogeometric beam formulation (“IGA, loc-r”), with  $p_d = p - 1$  and  $p_p = 1$ . Fig. 15 shows the convergence of the first four non-zero eigenvalues with increasing element number, for two different cases with degrees  $p = 2$  and  $p = 3$ . The reference solution

(“Ref.”) is obtained by numerically solving<sup>4</sup> the frequency equations for Euler-Bernoulli beam model, presented in Han et al. (1999). In all cases with  $p = 2$  and  $p = 3$ , the eigenfrequencies  $f_i := \omega_i/2\pi$  ( $i = 7, 8, 9, 10$ ) converge, and the converged values agree very well with the reference solutions.

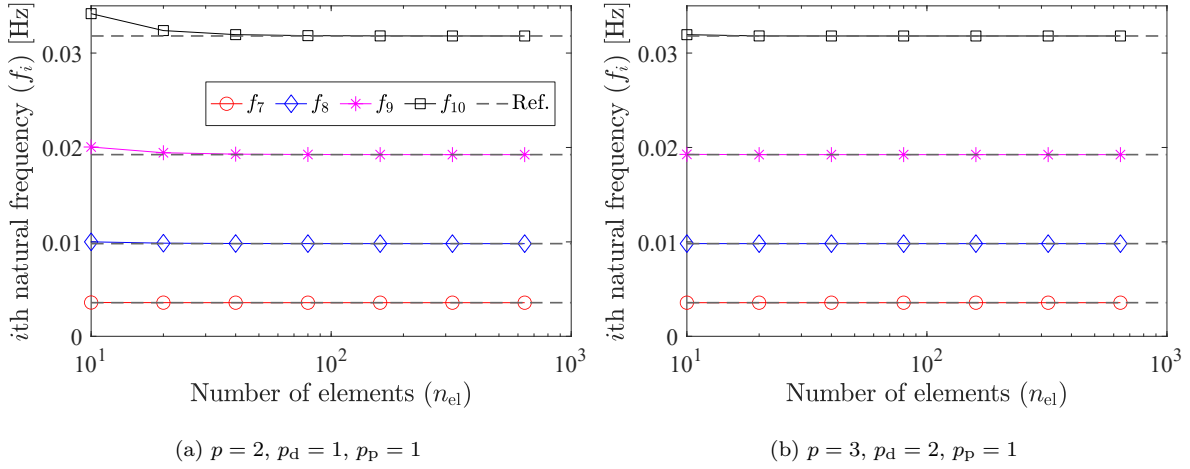


Figure 15: Eigenvalue analysis of a straight beam: Convergence of the first four non-zero eigenfrequencies,  $f_7 \sim f_{10}$ , with increasing number of elements (i.e.  $h$ -refinement). The generalized eigenvalue problem is solved at the initial configuration. The dashed lines (“Ref.”) represent the Euler-Bernoulli beam solution for each eigenmode, presented in Han et al. (1999).

Fig. 16 shows the convergence of the smallest four non-zero eigenfrequencies with increasing the degree of basis  $p$  and  $p_d = p - 1$ , for two different cases of element numbers,  $n_{el} = 10$  and 20. In both cases,  $p_p = 1$ . It is seen that the eigenfrequencies drastically decrease in very high degrees  $p \geq 8$ , which means that selecting those degrees may suffer from severe numerical instability, as we also observe in the result (red curve) of Fig. 13. However, as we increase the number of elements to  $n_{el} = 20$ , we obtain much better accuracy of  $f_8$  and  $f_9$ , which eventually leads to very accurate results even for those two degrees  $p = 8$  and 9 (cyan curve) in Fig. 13. For a further treatment of the locking and instability, one may consider an adjustment of the degree  $p_p$  *selectively*, in a similar way to the SRI method in Adam et al. (2014). This, together with a general test for stability in the mixed formulation (see e.g., the generalized inf-sup test in Krischok and Linder (2019)) remains future work.

<sup>4</sup>For this purpose, we use the function *fsolve* in MATLAB.

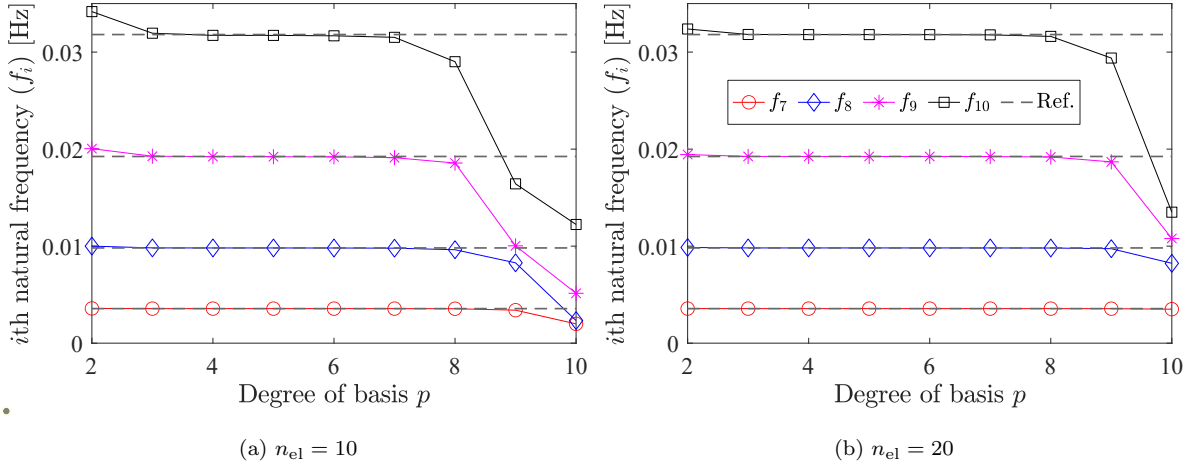


Figure 16: Eigenvalue analysis of a straight beam: Convergence of the first four non-zero eigenfrequencies,  $f_7 \sim f_{10}$ , with increasing degree  $p$  and  $p_d = p - 1$  (i.e.  $k$ -refinement). The generalized eigenvalue problem is solved at the initial configuration. The dashed lines (“Ref.”) represent the Euler-Bernoulli beam solution for each eigenmode, presented in Han et al. (1999).

#### 6.1.5. Improved convergence in the thin beam limit

We show that the advantage of the mixed formulation improves the convergence in the Newton-Raphson iteration. Table 1 compares the convergence history at the last load step between the displacement-based formulation with uniformly reduced integration (URI) and the mixed formulation. A very high slenderness ratio  $L/h = 10^5$  is considered. As seen, the mixed formulation needs much fewer iterations for the convergence than the displacement-based one. Further the mixed formulation shows monotonic convergence, but the displacement-based one exhibits severe oscillations during the iteration.

Table 1: Cantilever beam under bending moment: History of the Newton-Raphson iteration at the last (10th) load step, in case of the slenderness ratio  $L/h = 10^5$ .

Iteration#	Displacement-based formulation		Mixed formulation	
	FEA, $p = 2$ , $n_{el} = 10$ , URI		IGA, $p = 2$ , $n_{el} = 10$ , FI	
	Euclidean norm of residual	Energy norm	Euclidean norm of residual	Energy norm
1	6.3E-08	3.8E-08	6.3E-08	4.1E-08
2	4.1E+02	1.5E+02	4.8E+02	1.9E+02
3	5.6E+01	3.2E+00	2.3E+02	4.4E+01
4	2.1E+00	3.6E-03	7.7E+01	5.9E+00
5	3.9E-03	8.7E-09	1.2E+01	1.6E-01
6	4.0E-03	2.3E-08	2.8E-01	8.0E-05
7	2.8E-01	3.1E-05	4.6E-04	2.2E-10
8	6.5E-03	7.1E-08	1.5E-10	2.4E-23
⋮	⋮	⋮		
299	9.9E-05	1.8E-11		
300	1.5E-11	8.9E-19		
301	3.0E-09	1.6E-20		
302	1.5E-11	3.2E-26		

## 6.2. 45°-arc cantilever beam

We consider the initial beam center axis lying on the  $XY$ -plane and describing an 1/8 of a full circle with radius  $R = 100$  m and square cross-section of dimension  $h = w = 1$  m, see Fig. 17. One end face is fixed, and a distributed  $Z$ -directional force of  $\mathbf{F} = 600 \mathbf{e}_3$  [N/m<sup>2</sup>] is applied on the other end face. Two different cases with isotropic material properties are considered:

- Case 1: St. Venant-Kirchhoff type material without Poisson effect ( $\nu = 0$ ).
- Case 2: Compressible Neo-Hookean type material with Poisson effect,  $\nu = 0.3$ .

In both cases the Young's modulus is  $E = 10$  MPa. This example aims at verifying the following: (i) the improved agreement of the beam solution with the brick element one, due to the enriched cross-sectional strains, (ii) the robustness of the developed mixed finite element formulation in terms of stable Newton-Raphson convergence.

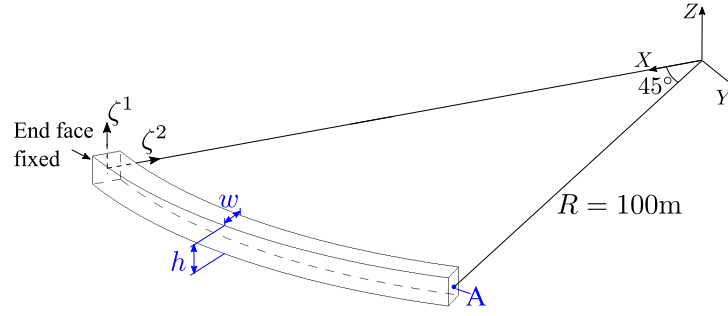


Figure 17: 45°-arc cantilever beam: Undeformed configuration and boundary conditions. Point A indicates the loaded end (tip) of center axis.

### 6.2.1. Case 1: Linear elastic material without Poisson effect

We compare the displacement at the tip of the center axis (point A in Fig. 17) with the brick element solution. For the IGA-based brick element solution, the following three different levels of mesh refinement in the cross-section is considered, with the same 320 NURBS elements (nonzero knot spans) along the center axis:

- a single linear element, i.e.  $\text{deg.} = (3, 1, 1)$ , and  $n_{\text{el}} = 320 \times 1 \times 1$ ,
- a single quadratic B-spline element, i.e.  $\text{deg.} = (3, 2, 2)$ , and  $n_{\text{el}} = 320 \times 1 \times 1$ ,
- $8 \times 8$  cubic B-spline elements, i.e.  $\text{deg.} = (3, 3, 3)$ , and  $n_{\text{el}} = 320 \times 8 \times 8$ .

Here, the notation  $\text{deg.} = (p_L, p_H, p_W)$ , and  $n_{\text{el}} = n_L \times n_H \times n_W$  denotes the degrees of basis functions, and the number of elements along the axial (L), and two transverse directions (H,W), respectively. Table C.1 shows the convergence of the brick element solution. In Table 2, we compare the tip displacements of the presented beam formulation with reference solutions from literature. It is noticeable that the presented beam formulation (“IGA, mixed, loc-r”) gives much better agreement with the brick element solution using a single quadratic element in the cross-section, compared with other reference solutions. However, it still deviates from the brick element solution with multiple elements in the cross-section (i.e. “IGA, brick,  $\text{deg.} = (3, 3, 3)$ ”). This can be further improved by enriching the higher order cross-sectional strains including the out-of-plane ones (cross-sectional warpings), which remains future work. It is seen that the enrichment of the linear and bilinear in-plane cross-sectional strains by the EAS method (i.e. “IGA, mixed, loc-r, EAS”) improves the agreement slightly.

Table 2: 45°-arc cantilever beam (case 1): Comparison of the tip displacements.

	$u_X$	$u_Y$	$u_Z$
IGA, brick, deg. = (3, 3, 3), $n_{el} = 320 \times 8 \times 8$	13.730631	-23.825817	53.609888
IGA, brick, deg. = (3, 1, 1), $n_{el} = 320 \times 1 \times 1$	13.604502	-23.568020	53.477701
IGA, brick, deg. = (3, 2, 2), $n_{el} = 320 \times 1 \times 1$	13.604269	-23.567644	53.477296
IGA, displacement-based, $p = 4$ , $n_{el} = 80$	13.604255	-23.567612	53.477268
IGA, mixed, (loc-r), $p = 4$ , $n_{el} = 80$	13.604255	-23.567611	53.477267
IGA, mixed, (loc-r, EAS), $p = 4$ , $n_{el} = 80$	13.604256	-23.567616	53.477273
<a href="#">Frischkorn and Reese (2013)</a>	14.11	-23.38	53.50
<a href="#">Rhim and Lee (1998)</a>	13.70	-23.64	53.46
<a href="#">Crisfield (1990)</a>	13.40	-23.50	53.40
<a href="#">Cardona and Geradin (1988)</a>	13.69	-23.87	53.71
<a href="#">Dvorkin et al. (1988)</a>	13.50	-23.48	53.37
<a href="#">Simo and Vu-Quoc (1986)</a>	13.74	-23.67	53.50
<a href="#">Bathe and Bolourchi (1979)</a>	13.60	-23.50	53.30

Further, Fig. 18 compares the convergence behavior between different finite element approximations of the independent solution fields, i.e. the global or local approach, and different degree of bases  $p$ ,  $p_d$ , and  $p_p$ . We utilize the relative difference in the tip displacement,

$$e_i^{\text{rel}} := \left| \frac{u_i^{\text{beam}} - u_i^{\text{brick}}}{u_i^{\text{brick}}} \right|, \quad i \in \{1, 2, 3\}, \quad (121)$$

where  $u_i^{\text{beam}}$  and  $u_i^{\text{brick}}$  denote the displacement component  $u_i := \mathbf{u} \cdot \mathbf{e}_i$  of the beam and brick elements, respectively. The black curves show the results from the global approach of the IGA-based mixed formulation (“glo”), which exhibits the highest level of accuracy among all the shown results, but is computationally very expensive. The blue curves show the results from the local approach of the IGA-based mixed formulation (“loc”) using the degree  $p_d = p$ , and  $p_p = p - 1$ . It is the same formulation as the global approach for a single element ( $n_{el} = 1$ ), so their results coincide then. However, as we increase the number of elements to  $n_{el} = 2$ , which has an interface between elements, “loc” suffers from a serious locking due to the  $C^{p-1}$  continuity condition in the displacement field, see the drastic increase of the relative difference in all components  $e_1^{\text{rel}}$ ,  $e_2^{\text{rel}}$ , and  $e_3^{\text{rel}}$ , as we increase  $n_{el}$  from 1 to 2. The red curves show the beam solutions with the IGA-based reduced local formulation (“loc-r”)  $p_d = p - 1$  and  $p_p = 1$ . It is seen that the reduction of  $p_d$  leads to significant locking due to the artificial couple shear strains, see the lower convergence rate in the red curves with circular markers (loc-r), compared with the results from using  $p_d = 2$  (blue curves with circular markers). However, in cases of higher  $p = 3, 4$ , and  $p_d = p - 1$  (red curves with triangle and square markers), the per DOF accuracy improves significantly, and shows much lower error, compared with the local approach (“loc”).

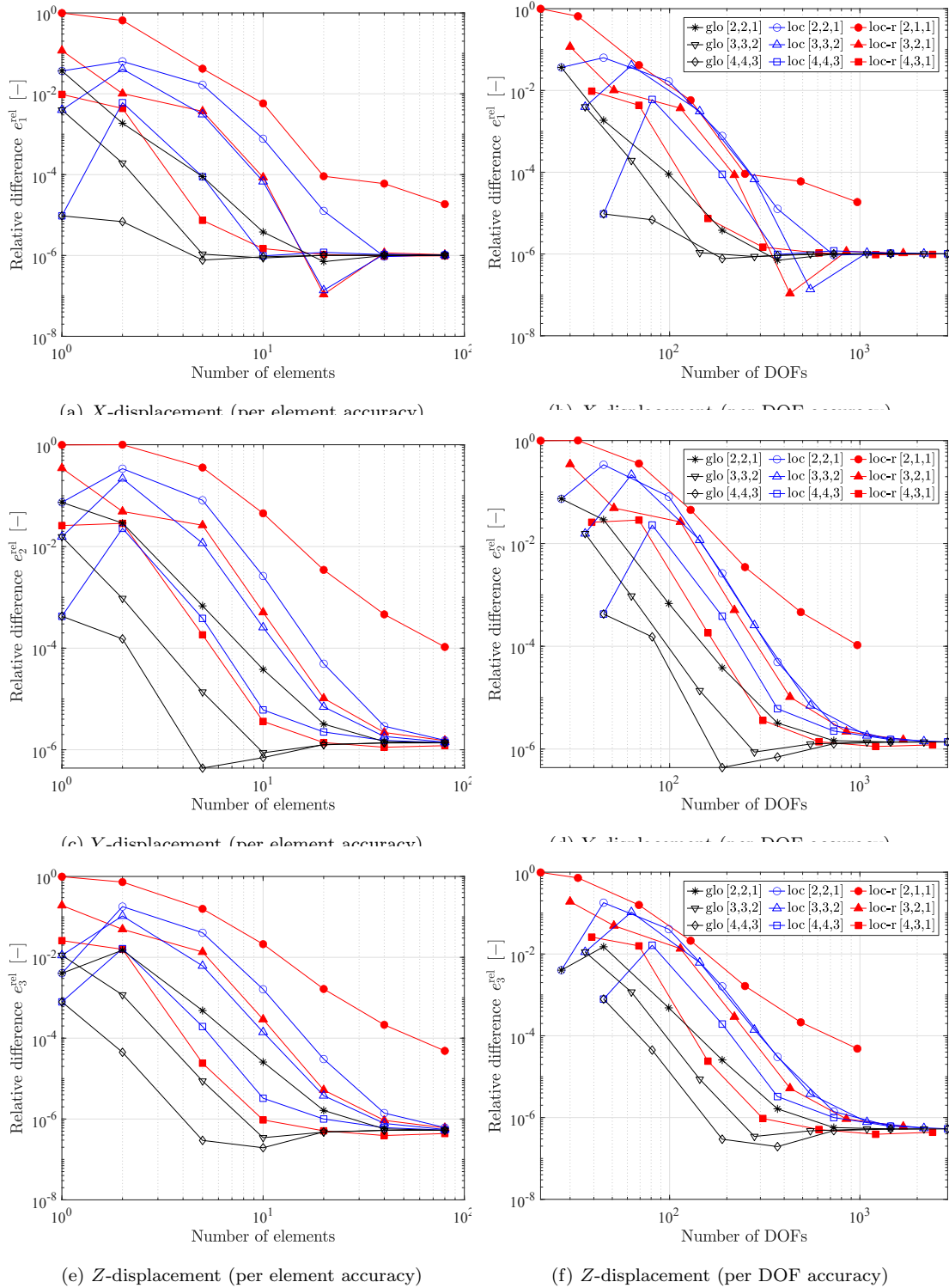


Figure 18: 45°-arc cantilever beam (Case 1): Relative difference of the displacement at the tip between beam and brick element solution. The latter is for a single quadratic B-spline element in the cross-section (i.e. “IGA, deg. = (3, 2, 2), and  $n_{el} = 320 \times 1 \times 1$ ”). The numbers in the bracket  $[\bullet]$  denotes the degrees,  $[p, p_d, p_p]$ . All the beam solutions are obtained by the IGA-based mixed formulation.

Table 3 shows that the presented mixed formulation allows much larger load steps, and eventually requires much fewer number of iterations, compared to various reference formulations, including the displacement-based one (i.e. “IGA, displacement-based”).

Table 3: 45°-arc cantilever beam (Case 1): Comparison of the number of load steps and Newton-Raphson iterations.

	#load steps	#iterations
IGA, mixed, (loc-r, EAS), $p = 4$ , $n_{el} = 80$	1	8
IGA, displacement-based, $p = 4$ , $n_{el} = 80$	1	18
IGA, brick, deg. = (3, 1, 1), $n_{el} = 320 \times 1 \times 1$	1	18
IGA, brick, deg. = (3, 2, 2), $n_{el} = 320 \times 1 \times 1$	1	18
Frischkorn and Reese (2013)	1	19
Wackerfuß and Gruttmann (2009)	1	9
Rhim and Lee (1998)	1	13
Crisfield (1990)	3	17
Cardona and Geradin (1988)	6	47
Dvorkin et al. (1988)	10	34
Simo and Vu-Quoc (1986)	3	27
Bathe and Bolourchi (1979)	60	-

We further show the path-independence of the proposed beam formulation employing the finite element approximation of the total displacements in the extensible directors. We investigate if the displacement at the tip (point A) vanishes after unloading. We also compare the results with those from the beam formulation of Simo and Vu-Quoc (1986). In the present paper, we approximate their field variables, displacement of the axis, and the incremental rotations by NURBS basis functions, in the framework of IGA, see Choi and Cho (2019) for more details. Fig. 19 shows the  $X$ -,  $Y$ - and  $Z$ -directional displacements at the tip after unloading. The beam formulation based on Simo and Vu-Quoc (1986) exhibits significant displacement error, which decreases with element number (black curves). In contrast, the proposed beam formulation yields vanishing displacements to machine precision, in both the displacement-based and the mixed formulations.

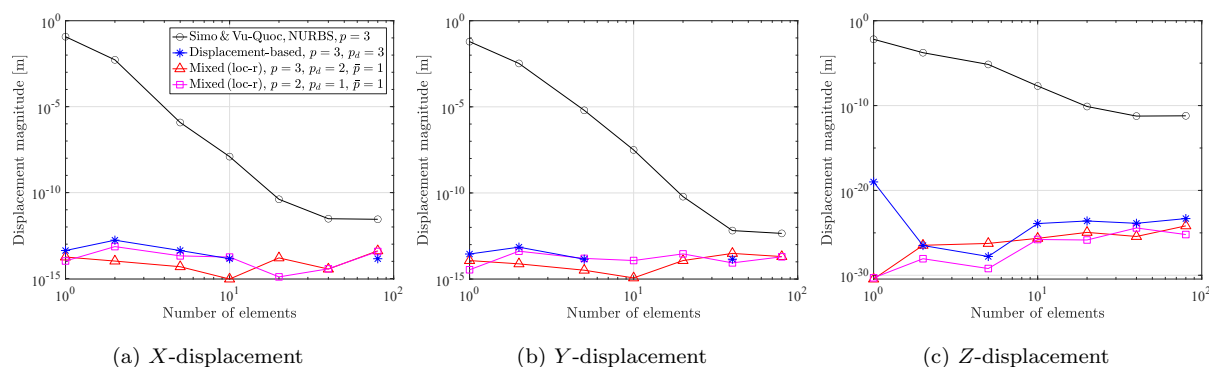


Figure 19: 45°-arc cantilever beam (Case 1): Displacement at the tip (point A) after unloading. All results are obtained by IGA. The missing data points in the blue curves in (a) and (b) are due to their values being exact zeros.



### 6.2.2. Case 2: nonlinear material with Poisson effect

In Case 2, we consider a compressible Neo-Hookean type material with Poisson's ratio  $\nu = 0.3$ , and Young's modulus  $E = 1.2 \times 10^7$  Pa. The same boundary conditions as in Case 1 are considered. Table 4 compares the displacement at the tip (point A in Fig. 17), with various brick element solutions. Severe artificial stiffening is observed in the brick element solution with a single linear quadrilateral element in the cross-section ("IGA, brick, deg. = (3, 1, 1),  $n_{el} = 320 \times 1 \times 1$ "), due to the lack of linear transverse normal strain, coupled with the bending deformation. The beam solution without any enrichment of the cross-sectional strains ("IGA, mixed, loc-r") suffers from even larger stiffening, since it lacks not only the quadratic but also the bilinear in-plane displacement field (i.e. trapezoidal cross-section deformations). After enriching the in-plane cross-sectional strains by the EAS method, the beam solution ("IGA, mixed, loc-r, EAS") shows a good agreement with the brick element solution based on a single quadratic element in the cross-section. Its deviation from the brick element solution using a single cubic element ("IGA brick deg. = (3, 3, 3),  $n_{el} = 320 \times 1 \times 1$ ") shows the significance of the cross-sectional warping effect, which our current beam formulation does not account for. This remains future work.

Table 4: 45°-arc cantilever beam (Case 2): Comparison of the tip displacements.

	$u_1$ [m]	$u_2$ [m]	$u_3$ [m]
IGA brick deg. = (3, 1, 1), $n_{el} = 320 \times 1 \times 1$	12.5816	-21.6881	51.5348
IGA brick deg. = (3, 2, 2), $n_{el} = 320 \times 1 \times 1$	13.8087	-23.9547	53.6642
IGA brick deg. = (3, 3, 3), $n_{el} = 320 \times 1 \times 1$	13.9947	-24.2610	53.8291
IGA, mixed (loc-r), $p = 4$ , $p_d = 3$ , $p_p = 1$ , $n_{el} = 80$	11.3090	-19.3285	49.1188
IGA, mixed (loc-r, EAS), $p = 4$ , $p_d = 3$ , $p_p = 1$ , $n_{el} = 80$	13.8148	-23.9790	53.6901

In Fig. 20, we compare the convergence of the relative difference in the tip displacements,  $e_i^{rel}$  in Eq. (121), between several different finite element approximations for independent solution fields. As observed in Case 1, the results from using  $p = 2$ , and  $p_d = p - 1 = 1$  exhibit severe locking due to the spurious couple shear strain (red curves with circular markers), in comparison to the results from the same degree  $p = 2$  with higher degree  $p_d = p = 2$  (blue curves with circular markers). However, in the cases of higher  $p = 3, 4$  and  $p_d = p - 1$  (red curves with triangle and square markers), the accuracy improvement is noticeable.

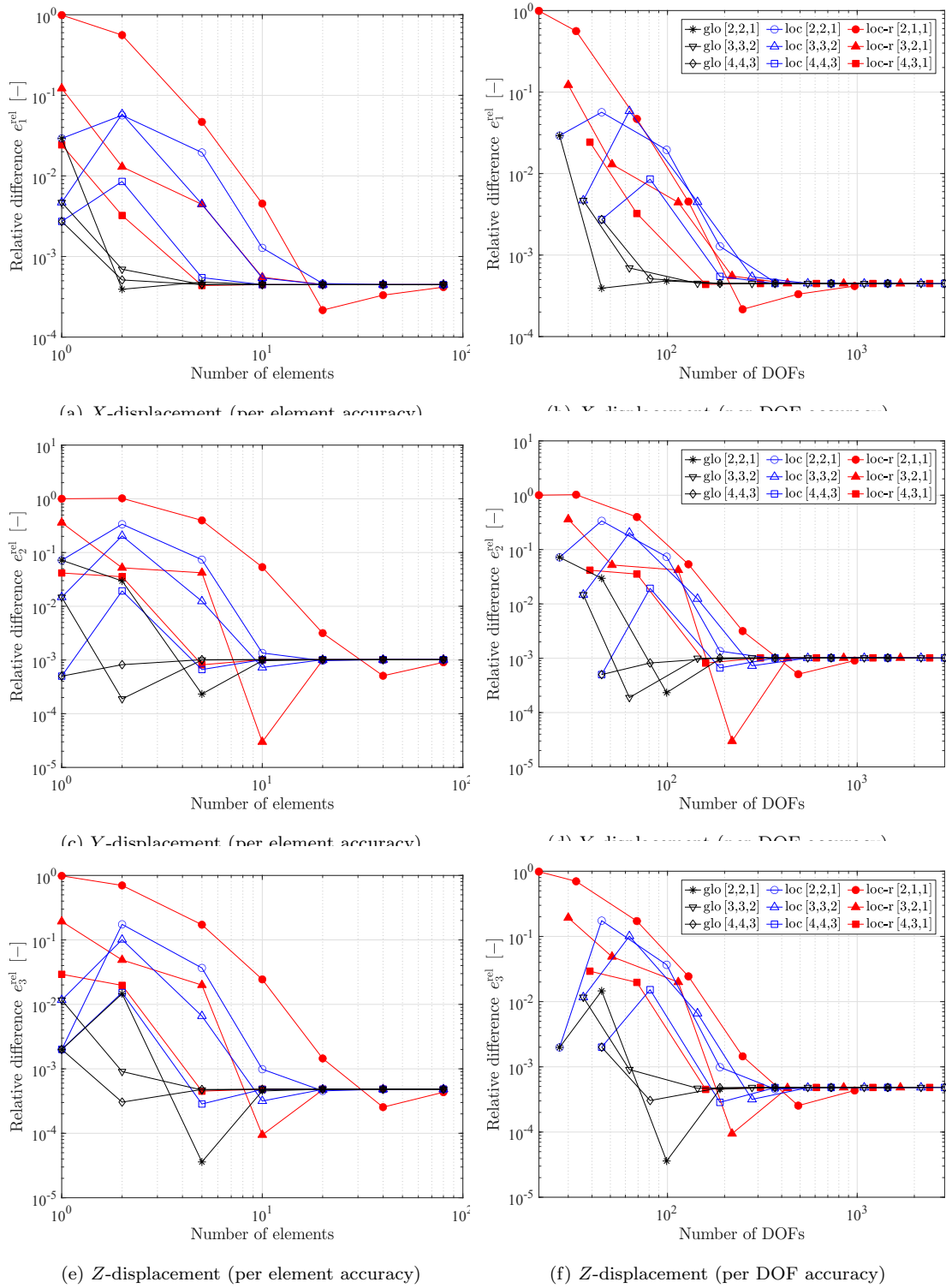


Figure 20: 45°-arc cantilever beam (Case 2): Relative difference of the displacement at the tip between beam and brick element solution. The latter is for a single quadratic B-spline element in the cross-section (i.e. “IGA, deg. = (3, 2, 2), and  $n_{el} = 320 \times 1 \times 1$ ”). The numbers in the bracket  $[\bullet]$  denotes the degrees,  $[p, p_a, p_p]$ . All the beam solutions are obtained by the IGA-based mixed formulation.

### 6.3. L-shape frame

In this example, we show the path-independence of the presented mixed isogeometric beam formulation, considering two beams connected by a rotational continuity condition. We consider a L-shape

frame with two straight beams having the initial length  $L = 10$  m and a square cross-section of dimension  $h = w = 0.5$  m. We select compressible Neo-Hookean type material with Young's modulus  $E = 10^7$  Pa and Poisson's ratio  $\nu = 0.3$ . A distributed force  $\bar{T}_0 = -200$  N/m is applied in  $Z$ -direction on the upper edge of the end face, and the other end is fixed, see Fig. 21. The load is applied in five load steps with uniform increments. In order to test the path-independence of the beam formulation, we impose a prescribed rotation at the fixed end keeping the applied load fixed, such that the force maintains the negative  $Z$ -direction, and does not rotate along  $\bar{\theta}$ . This procedure is inspired by a similar test in Ibrahimbegovic and Taylor (2002). The rotation is prescribed about the  $X$ -axis, and we choose the total rotation angle  $\bar{\theta} = 200\pi$ , i.e. 100 turns around the  $X$ -axis. In the additional prescribed rotation, we use  $10^3$  load steps in total, such that each full ( $360^\circ$ ) turn is uniformly divided by 10 increments, i.e.  $36^\circ$  rotation is prescribed in each load step. Here, all the results are obtained by the proposed isogeometric mixed formulation ("IGA-r") with  $p = 3$ ,  $p_d = 2$ ,  $p_p = 1$ . We also use  $n_{el} = 5$  for each beam, so that we have 10 elements in total.

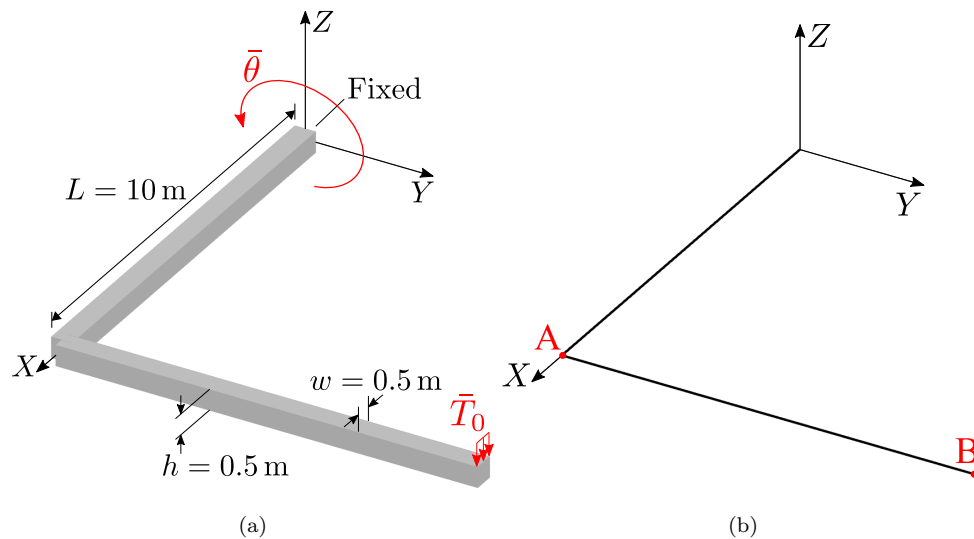
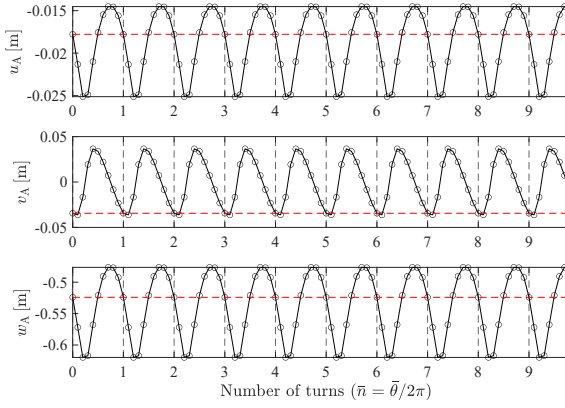
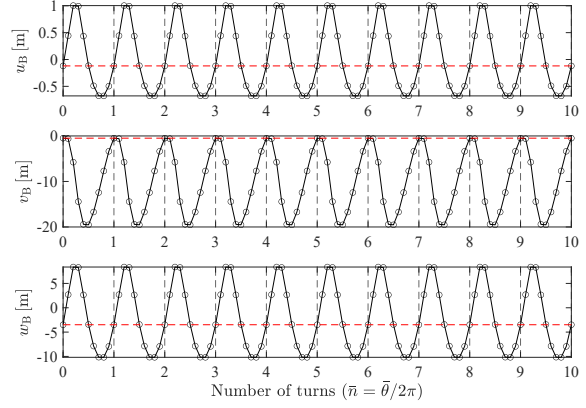


Figure 21: L-shape frame. (a) Undeformed configuration and boundary conditions. (b) Center axes of two connected beams, where A and B indicate selected points where displacements are evaluated to test path-independence.

Fig. 22 shows a periodic change of the displacements at the points A and B along the turns. Here,  $u$ ,  $v$ , and  $w$  indicate the  $X$ -,  $Y$ -, and  $Z$ -displacements, respectively. It is seen that the displacement at every full turn exhibits the same value, which demonstrates the path-independence of our beam formulation. For a more thorough investigation, in Fig. 23, we plot the change of the displacements at points A and B along the 100 full turns.  $u_A^0$ ,  $v_A^0$ , and  $w_A^0$  denote the displacements due to the applied force  $\bar{T}_0$  at  $\bar{\theta} = 0$ . For all displacement components, the difference vanishes up to machine precision. A linearly increasing small error is due to the accumulated numerical error by the limited machine precision.

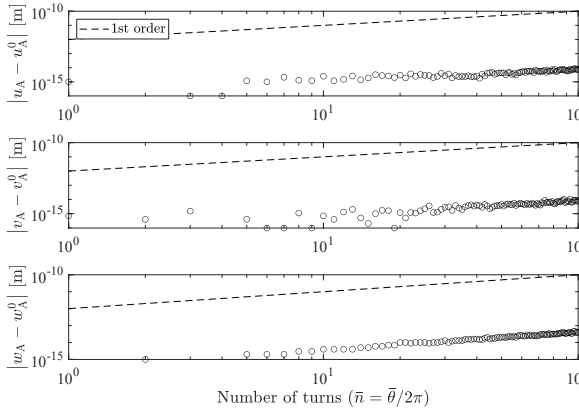


(a) Displacement at A

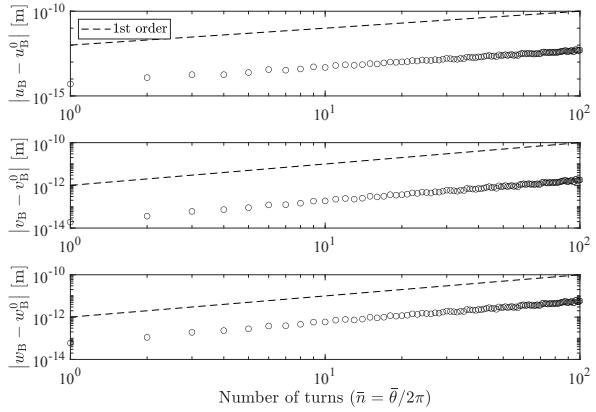


(b) Displacement at B

Figure 22: L-shape frame: Displacements at points A and B due to the additional prescribed rotation. The horizontal red dashed line marks the displacements at the deformed configuration by the applied force  $\bar{T}_0$  and  $\bar{\theta} = 0$ , and the vertical dashed lines mark every full turn, i.e.  $\bar{n} := \bar{\theta}/2\pi = 1, 2, \dots, 10$ .



(a) Displacements at A



(b) Displacements at B

Figure 23: L-shape frame. Difference of displacements at point A and B due to the additional prescribed rotations  $\bar{\theta} = 2\bar{n}\pi$  with  $\bar{n} = 1, 2, \dots, 100$ . The subscript A and B denote the displacements at point A and B, respectively, and the superscript 0 denotes the displacements at the turn number  $\bar{n} = 0$ .

## 7. Conclusion

This paper presents an isogeometric mixed finite element formulation for nonlinear beams with extensible directors. We particularly investigate a selective reduction of the degree of bases for the independent solution fields of axis displacement, directors, and additional stress and strain fields. We propose to use  $p_d = p - 1$  and  $p_p = 1$ , for all degrees  $p \geq 2$ . This approach effectively alleviates additional locking phenomena due to the higher order continuity of the displacement field in IGA. Based on this, we show the superior per DOF accuracy of IGA over conventional FEA. Further the developed method is computationally efficient, due to its local (element-wise) static condensation process, and the symmetry of the tangent stiffness matrix under conservative loads, and much less internal DOFs due to the reduced degree of bases. It is also shown that the mixed formulation yields improved convergence in the Newton-Raphson iteration in the thin beam limit, compared to the displacement-based one. Important

extensions of this work are expected in the following directions:

- Further investigation on the numerical stability in proposed selection of degree  $p_p = 1$ , based on a generalized inf-sup test for multi-field variational principle, e.g. see [Krischok and Linder \(2019\)](#),
- An optimal selection of degrees for  $p_p$  for each component of the beam strain and stress resultant,
- Further enhancement of the out-of-plane cross-sectional strain including the torsion-induced warping effect.

## A. Appendix to the beam formulation

### A.1. Operator expressions in geometric tangent stiffness part

In Eq. (58a), we utilize the following operators from [Choi et al. \(2021\)](#) with the original stress resultants replaced by the physical (independent) stress resultants.

$$\mathbf{k}_G := \begin{bmatrix} \mathbf{k}_\varepsilon & \mathbf{k}_\rho & \mathbf{k}_\delta \\ & \mathbf{k}_\kappa & \mathbf{k}_\gamma \\ \text{sym.} & & \mathbf{k}_\chi \end{bmatrix}_{15 \times 15}, \quad (\text{A.1.1})$$

with

$$\mathbf{k}_\varepsilon := \tilde{n}_p \mathbf{1}_{3 \times 3}, \quad (\text{A.1.2a})$$

$$\mathbf{k}_\rho := \begin{bmatrix} \tilde{m}_p^1 \mathbf{1}_{3 \times 3} & \tilde{m}_p^2 \mathbf{1}_{3 \times 3} \end{bmatrix}, \quad (\text{A.1.2b})$$

$$\mathbf{k}_\delta := \begin{bmatrix} \tilde{q}_p^1 \mathbf{1}_{3 \times 3} & \tilde{q}_p^2 \mathbf{1}_{3 \times 3} \end{bmatrix}, \quad (\text{A.1.2c})$$

$$\mathbf{k}_\kappa := \begin{bmatrix} \tilde{h}_p^{11} \mathbf{1}_{3 \times 3} & \tilde{h}_p^{12} \mathbf{1}_{3 \times 3} \\ \text{sym.} & \tilde{h}_p^{22} \mathbf{1}_{3 \times 3} \end{bmatrix}, \quad (\text{A.1.2d})$$

$$\mathbf{k}_\gamma := \begin{bmatrix} \tilde{m}_p^{11} \mathbf{1}_{3 \times 3} & \tilde{m}_p^{21} \mathbf{1}_{3 \times 3} \\ \tilde{m}_p^{12} \mathbf{1}_{3 \times 3} & \tilde{m}_p^{22} \mathbf{1}_{3 \times 3} \end{bmatrix}, \quad (\text{A.1.2e})$$

$$\mathbf{k}_\chi := \begin{bmatrix} \tilde{l}_p^{11} \mathbf{1}_{3 \times 3} & \tilde{l}_p^{21} \mathbf{1}_{3 \times 3} \\ \text{sym.} & \tilde{l}_p^{22} \mathbf{1}_{3 \times 3} \end{bmatrix}, \quad (\text{A.1.2f})$$

and  $\mathbb{Y}_e := \begin{bmatrix} \mathbf{Y}_1 & \cdots & \mathbf{Y}_{n_e} \end{bmatrix}_{15 \times 9n_e}$ , with

$$\mathbf{Y}_I := \begin{bmatrix} N_{I,s} \mathbf{1}_{3 \times 3} & \mathbf{0}_{3 \times 3} & \mathbf{0}_{3 \times 3} \\ \mathbf{0}_{3 \times 3} & N_{I,s} \mathbf{1}_{3 \times 3} & \mathbf{0}_{3 \times 3} \\ \mathbf{0}_{3 \times 3} & \mathbf{0}_{3 \times 3} & N_{I,s} \mathbf{1}_{3 \times 3} \\ \mathbf{0}_{3 \times 3} & N_I \mathbf{1}_{3 \times 3} & \mathbf{0}_{3 \times 3} \\ \mathbf{0}_{3 \times 3} & \mathbf{0}_{3 \times 3} & N_I \mathbf{1}_{3 \times 3} \end{bmatrix}_{15 \times 9}. \quad (\text{A.1.3})$$

### A.2. Imposition of rotational continuity between beams

Table A.1 shows the global control coefficient index  $K$  for the director displacement field, corresponding to given the local coefficient index  $I$  in  $e$ th element, in two different cases of the location of junction.

Table A.1: Two cases of the joint condition: Correspondence between the local coefficient index  $I$  in  $e$ th element, and the global coefficient index  $K$ .

	Element number $e$	Local index $I$	Global index $K$
Case 1	1	1	1
Case 2	$n_{\text{el}}$	$n_e$	$n_{\text{cp}}^{\text{d}}$

## B. Appendix: Consistent mass matrix

We have the kinetic energy bilinear form for a three-dimensional body, as

$$d(\mathbf{x}, \delta \mathbf{x}) = \int_{\mathcal{B}} \rho_0 \delta \mathbf{x} \cdot \mathbf{x}_{,tt} j_0 \, d\mathcal{B}, \quad (\text{B.0.1})$$

where  $\mathbf{x}_{,tt}$  denotes the second order derivative of the material point position  $\mathbf{x}$  with respect to the time  $t$ . The increment of the kinetic energy form is simply obtained by

$$\Delta d(\mathbf{x}, \delta \mathbf{x}) = d(\Delta \mathbf{x}, \delta \mathbf{x}) = \int_{\mathcal{B}} \rho_0 \delta \mathbf{x} \cdot \Delta \mathbf{x}_{,tt} j_0 \, d\mathcal{B}. \quad (\text{B.0.2})$$

Applying the beam kinematics, we have

$$d(\Delta \mathbf{y}, \delta \mathbf{y}) = \int_0^L \delta \mathbf{y}^{\text{T}} \mathbf{I}_\rho \Delta \mathbf{y} \, ds, \quad (\text{B.0.3})$$

where  $\mathbf{I}_\rho$  is an inertia matrix, defined by

$$\mathbf{I}_\rho = \begin{bmatrix} \rho_A \mathbf{1}_3 & \mathbf{0}_{3 \times 3} & \mathbf{0}_{3 \times 3} \\ & I_\rho^{11} \mathbf{1}_3 & I_\rho^{12} \mathbf{1}_3 \\ \text{sym.} & & I_\rho^{22} \mathbf{1}_3 \end{bmatrix}, \quad (\text{B.0.4})$$

with

$$I_\rho^{\gamma\delta} = \int_A \rho_0 \zeta^\gamma \zeta^\delta j_0 \, dA. \quad (\text{B.0.5})$$

It should be noted that the inertia matrix is constant during deformation, and it depends only on the initial geometry and the initial mass density distribution. Applying the spatial discretization using NURBS basis functions, we have

$$d(\Delta \mathbf{y}^h, \delta \mathbf{y}^h) = \delta \mathbf{y}^{\text{T}} \mathbf{M} \Delta \mathbf{y}, \quad \text{with } \mathbf{M} := \sum_{e=1}^{n_{\text{el}}} \mathbf{A}^e \mathbf{m}^e, \quad (\text{B.0.6})$$

where the element mass matrix is obtained as

$$\mathbf{m}^e := \int_{\Xi^e} \mathbf{N}^e(\xi)^{\text{T}} \mathbf{I}_\rho \mathbf{N}^e(\xi) \tilde{j} \, d\xi. \quad (\text{B.0.7})$$

Note that the mass matrix is constant in deformation.

## C. Appendix to numerical examples

### C.1. 45°-arc cantilever beam

Table C.1 presents the convergence test results of the brick element solution of the tip displacement for Case 1.

Table C.1: 45°-arc cantilever beam (Case 1): In all cases, we use IGA.

Brick, deg. = (3, 3, 3)	Tip displacements			
	$n_{el}$	$u_X$ [m]	$u_Y$ [m]	$u_Z$ [m]
$1 \times 40 \times 1$		1.3729E+01	-2.3822E+01	5.3607E+01
$1 \times 80 \times 1$		1.3730E+01	-2.3825E+01	5.3609E+01
$1 \times 160 \times 1$		1.3731E+01	-2.3826E+01	5.3610E+01
$5 \times 240 \times 5$		1.3731E+01	-2.3826E+01	5.3610E+01
$8 \times 240 \times 8$		1.3731E+01	-2.3826E+01	5.3610E+01
$8 \times 320 \times 8$		1.3731E+01	-2.3826E+01	5.3610E+01

### Acknowledgement

M.-J. Choi would like to gratefully acknowledge the financial support of a postdoctoral research fellowship from the Alexander von Humboldt Foundation in Germany.

### References

- C. Cyron, W. A. Wall, Numerical method for the simulation of the Brownian dynamics of rod-like microstructures with three-dimensional nonlinear beam elements, *International Journal for Numerical Methods in Engineering* 90 (2012) 955–87.
- M. G. Schmidt, A. E. Ismail, R. A. Sauer, A continuum mechanical surrogate model for atomic beam structures, *International Journal for Multiscale Computational Engineering* 13 (2015).
- D. Durville, Numerical simulation of entangled materials mechanical properties, *Journal of Materials Science* 40 (2005) 5941–8.
- C. Meier, A. Popp, W. A. Wall, Geometrically exact finite element formulations for slender beams: Kirchhoff–Love theory versus Simo–Reissner theory, *Archives of Computational Methods in Engineering* 26 (2019) 163–243.
- M.-J. Choi, R. A. Sauer, S. Klinkel, An isogeometric finite element formulation for geometrically exact Timoshenko beams with extensible directors, *Computer Methods in Applied Mechanics and Engineering* 385 (2021) 113993.
- T. J. R. Hughes, J. A. Cottrell, Y. Bazilevs, Isogeometric analysis: CAD, finite elements, NURBS, exact geometry and mesh refinement, *Computer Methods in Applied Mechanics and Engineering* 194 (2005) 4135–95.

- T. J. R. Hughes, A. Reali, G. Sangalli, Duality and unified analysis of discrete approximations in structural dynamics and wave propagation: comparison of p-method finite elements with k-method NURBS, *Computer Methods in Applied Mechanics and Engineering* 197 (2008) 4104–24.
- J. A. Cottrell, A. Reali, Y. Bazilevs, T. J. R. Hughes, Isogeometric analysis of structural vibrations, *Computer Methods in Applied Mechanics and Engineering* 195 (2006) 5257–96.
- R. Echter, M. Bischoff, Numerical efficiency, locking and unlocking of NURBS finite elements, *Computer Methods in Applied Mechanics and Engineering* 199 (2010) 374–82.
- C. Adam, S. Bouabdallah, M. Zarroug, H. Maitournam, Improved numerical integration for locking treatment in isogeometric structural elements, Part I: Beams, *Computer Methods in Applied Mechanics and Engineering* 279 (2014) 1–28.
- G. Prathap, The finite element method in structural mechanics: principles and practice of design of field-consistent elements for structural and solid mechanics, volume 24, Springer Science & Business Media, 2013.
- R. Bouclier, T. Elguedj, A. Combescure, Locking free isogeometric formulations of curved thick beams, *Computer Methods in Applied Mechanics and Engineering* 245 (2012) 144–62.
- P. Hu, Q. Hu, Y. Xia, Order reduction method for locking free isogeometric analysis of Timoshenko beams, *Computer Methods in Applied Mechanics and Engineering* 308 (2016) 1–22.
- Q. Hu, Y. Xia, S. Natarajan, A. Zilian, P. Hu, S. P. Bordas, Isogeometric analysis of thin Reissner–Mindlin shells: locking phenomena and B-bar method, *Computational Mechanics* 65 (2020) 1323–41.
- T. J. R. Hughes, A. Reali, G. Sangalli, Efficient quadrature for NURBS-based isogeometric analysis, *Computer Methods in Applied Mechanics and Engineering* 199 (2010) 301–13.
- C. Adam, T. J. R. Hughes, S. Bouabdallah, M. Zarroug, H. Maitournam, Selective and reduced numerical integrations for nurbs-based isogeometric analysis, *Computer Methods in Applied Mechanics and Engineering* 284 (2015) 732–61.
- Z. Zou, T. J. R. Hughes, M. A. Scott, D. Miao, R. A. Sauer, Efficient and robust quadratures for isogeometric analysis: Reduced Gauss and Gauss–Greville rules, *Computer Methods in Applied Mechanics and Engineering* 392 (2022) 114722.
- S. Govindjee, J. Strain, T. J. Mitchell, R. L. Taylor, Convergence of an efficient local least-squares fitting method for bases with compact support, *Computer Methods in Applied Mechanics and Engineering* 213 (2012) 84–92.
- R. Bouclier, T. Elguedj, A. Combescure, Efficient isogeometric NURBS-based solid-shell elements: Mixed formulation and B-method, *Computer Methods in Applied Mechanics and Engineering* 267 (2013) 86–110.



- L. Greco, M. Cuomo, L. Contrafatto, S. Gazzo, An efficient blended mixed B-spline formulation for removing membrane locking in plane curved Kirchhoff rods, *Computer Methods in Applied Mechanics and Engineering* 324 (2017) 476–511.
- G. Kikis, S. Klinkel, Two-field formulations for isogeometric Reissner–Mindlin plates and shells with global and local condensation, *Computational Mechanics* (2022) 1–21.
- E. Marino, Locking-free isogeometric collocation formulation for three-dimensional geometrically exact shear-deformable beams with arbitrary initial curvature, *Computer Methods in Applied Mechanics and Engineering* 324 (2017) 546–72.
- O. Weeger, S.-K. Yeung, M. L. Dunn, Isogeometric collocation methods for cosserat rods and rod structures, *Computer Methods in Applied Mechanics and Engineering* 316 (2017) 100–22.
- L. B. Da Veiga, A. Buffa, C. Lovadina, M. Martinelli, G. Sangalli, An isogeometric method for the Reissner–Mindlin plate bending problem, *Computer Methods in Applied Mechanics and Engineering* 209 (2012) 45–53.
- G. Kikis, W. Dornisch, S. Klinkel, Adjusted approximation spaces for the treatment of transverse shear locking in isogeometric Reissner–Mindlin shell analysis, *Computer Methods in Applied Mechanics and Engineering* 354 (2019) 850–70.
- P. Betsch, E. Stein, An assumed strain approach avoiding artificial thickness straining for a non-linear 4-node shell element, *Communications in Numerical Methods in Engineering* 11 (1995) 899–909.
- S. Klinkel, F. Gruttmann, W. Wagner, A robust non-linear solid shell element based on a mixed variational formulation, *Computer Methods in Applied Mechanics and Engineering* 195 (2006) 179–201.
- H. Santos, P. Pimenta, J. M. De Almeida, Hybrid and multi-field variational principles for geometrically exact three-dimensional beams, *International Journal of Non-Linear Mechanics* 45 (2010) 809–20.
- J. Rhim, S. W. Lee, A vectorial approach to computational modelling of beams undergoing finite rotations, *International Journal for Numerical Methods in Engineering* 41 (1998) 527–40.
- J. C. Simo, M. Rifai, A class of mixed assumed strain methods and the method of incompatible modes, *International Journal for Numerical Methods in Engineering* 29 (1990) 1595–638.
- J. Wackerfuß, F. Gruttmann, A mixed hybrid finite beam element with an interface to arbitrary three-dimensional material models, *Computer Methods in Applied Mechanics and Engineering* 198 (2009) 2053–66.
- J. Wackerfuß, F. Gruttmann, A nonlinear Hu–Washizu variational formulation and related finite-element implementation for spatial beams with arbitrary moderate thick cross-sections, *Computer Methods in Applied Mechanics and Engineering* 200 (2011) 1671–90.
- L. Piegl, W. Tiller, *The NURBS book*, Springer Science & Business Media, 1996.

- I. Romero, F. Armero, An objective finite element approximation of the kinematics of geometrically exact rods and its use in the formulation of an energy–momentum conserving scheme in dynamics, *International Journal for Numerical Methods in Engineering* 54 (2002) 1683–716.
- J. C. Simo, D. D. Fox, On a stress resultant geometrically exact shell model. part I: Formulation and optimal parametrization, *Computer Methods in Applied Mechanics and Engineering* 72 (1989) 267–304.
- J. C. Simo, L. Vu-Quoc, A three-dimensional finite-strain rod model. part II: Computational aspects, *Computer Methods in Applied Mechanics and Engineering* 58 (1986) 79–116.
- J. Argyris, An excursion into large rotations, *Computer Methods in Applied Mechanics and Engineering* 32 (1982) 85–155.
- S. M. Han, H. Benaroya, T. Wei, Dynamics of transversely vibrating beams using four engineering theories, *Journal of Sound and Vibration* 225 (1999) 935–88.
- A. Krischok, C. Linder, A generalized inf–sup test for multi-field mixed-variational methods, *Computer Methods in Applied Mechanics and Engineering* 357 (2019) 112497.
- J. Frischkorn, S. Reese, A solid-beam finite element and non-linear constitutive modelling, *Computer Methods in Applied Mechanics and Engineering* 265 (2013) 195–212.
- M. A. Crisfield, A consistent co-rotational formulation for non-linear, three-dimensional, beam-elements, *Computer Methods in Applied Mechanics and Engineering* 81 (1990) 131–50.
- A. Cardona, M. Geradin, A beam finite element non-linear theory with finite rotations, *International Journal for Numerical Methods in Engineering* 26 (1988) 2403–38.
- E. N. Dvorkin, E. Oñate, J. Oliver, On a non-linear formulation for curved timoshenko beam elements considering large displacement/rotation increments, *International Journal for Numerical Methods in Engineering* 26 (1988) 1597–613.
- K.-J. Bathe, S. Bolourchi, Large displacement analysis of three-dimensional beam structures, *International Journal for Numerical Methods in Engineering* 14 (1979) 961–86.
- M.-J. Choi, S. Cho, Isogeometric configuration design sensitivity analysis of geometrically exact shear-deformable beam structures, *Computer Methods in Applied Mechanics and Engineering* 351 (2019) 153–83.
- A. Ibrahimbegovic, R. L. Taylor, On the role of frame-invariance in structural mechanics models at finite rotations, *Computer Methods in Applied Mechanics and Engineering* 191 (2002) 5159–76.

